pH-dependent structural changes of arsenic oxoacids in solution and solid phase: Raman spectrometry and computational studies

F.J. Pereira[1,*], R. López[1], D. Suarez[2] and A.J. Aller[1]

[1]*Department of Applied Chemistry and Physics, Faculty of Biological and Environmental Sciences, Campus de Vegazana, s/n, University of León, E-24071 León, Spain, E-mail:* FJP: *fjperg@unileon.es*

[2]*Department of Physical and Analytical Chemistry, Area of Physical Chemistry, Faculty of Chemistry, Julián Clavería 8, University of Oviedo, E-33006 Oviedo, Spain*

Highlights

• Speciation of arsenic oxoacids in aqueous solutions is possible by Raman spectrometry.

• The Raman spectra of the dry solid phases do not always correlate with the arsenic oxoacids in the solution.

• The computational study models well the experimental Raman shifts of arsenic oxoacids in solution.

• The intensity of some Raman peaks relates directly to the $As^{(III)}$ oxoacids concentration in solution.

• Identification of the arsenic oxoacids in solution is possible through a fine selection of the Raman peaks of the dry solid phases.

Abstract

Reliably knowledge of the arsenic oxoacids in solution and solid-state and any possible relationship between them at different pHs is of concern in various scientific fields. This work compares the experimental Raman spectra of the inorganic arsenic oxoacids in aqueous solutions under acidic, neutral and alkaline conditions with the dry precipitates obtained from the corresponding aqueous solutions. Further, we explore the ability of quantum chemical methods to model the Raman spectra of the arsenic oxoacids in solution by considering explicit water molecules and conformational sampling, fitting reasonably well with the experimental spectra in the whole pH range covered. Hydrogen bridges and the coexistence of arsenic oxoacids facilitate strong overlapping in the Raman spectra of the $As^{(III)}$ aqueous samples compared with the $As^{(V)}$ ones. Some Raman shifts of the dry arsenic precipitates correlate well with the corresponding Raman spectra of the same arsenic species in aqueous solutions, allowing a practical use of the Raman spectrometry for indirect screening purposes of arsenic speciation in both condensed phases.

Keywords: Arsenic oxoacids; Speciation; Solid-phase; Raman spectrometry; Computational studies

1. Introduction

Inorganic arsenic oxoacids usually represent the last step in a degradative oxidation process of any arsenic compound, exhibiting high activity in various environmental and biological systems. The stability of inorganic arsenic species depends on the Eh-pH conditions,

although several arsenic oxoacids in solution and solid-phase can coexist. Under oxidant conditions, the following $As^{(V)}$ species, H_3AsO_4, $H_2AsO_4^-$, $HAsO_4^{2-}$ and AsO_4^{3-} predominate sequentially from acidic to alkaline conditions. Contrarily, under reducing (or anoxic) conditions, primary $As^{(III)}$ species include H_3AsO_3, $H_2AsO_3^-$, $HAsO_3^{2-}$ and AsO_3^{3-} among the most abundant. Nonetheless, in aqueous solution and depending on pH and arsenic concentration, other oxygenated $As^{(III)}$ species, such as *ortho-* (isolated AsO_3^{3-} species), *pyro-* (dimers or $As_2O_5^{4-}$ species), or *meta-* (several connected AsO_2^- species) configurations ($HAsO_2 + H_2O \leftrightarrow H_3AsO_3$) can also be theoretically present [1]. Similarly, solid arsenic oxoacids show different polymorphisms (crystalline structures), which are adequate to form adamantanoid cages, raising tremendous interest as solid models in many industrial and medicinal applications [2,3]. Thus, the typical solid arsenic trioxide As_2O_3, containing unstable arsenious acid, has As_4O_6 units, which may be present as vitreous (unclear structure), arsenolite (cubic crystalline of As_4O_6 'dimers' forming an adamantanoid cage with T_d symmetry), and claudetite I or claudetite II (monoclinic As_2O_3) phases [4].

As much in solid phase as in aqueous media at different pHs, accurate knowledge about the As oxoacids is of great concern in diverse biogeochemistry processes for environmental and biological studies. Further, stability studies of the As oxoacids are critical in toxicological evaluations. Following this trend, experimental and computational studies of the stability of hydrolytic $As^{(III)}$ and $As^{(V)}$ species in aqueous solution under different pH conditions have been reported [5]. Cassone et al. [5] found H_3AsO_4, $H_2AsO_4^-$, $HAsO_4^{2-}$ and AsO_4^{3-} from $As^{(V)}$ solutions and H_3AsO_3 and $H_2AsO_3^-$ from $As^{(III)}$ solutions as the most relevant oxoacids species in biological and environmental samples at pH 2-11. Furthermore, Raman spectra of $As^{(III)}$ and $As^{(V)}$ species in aqueous solutions, as well as sorbed on iron oxide at various pHs, have also been evaluated for separation purposes [6]. However, despite the previous studies about the As oxoacid, there are still uncertainties in identifying and modelling the arsenic species present in

any aggregation state, requiring a better understanding of their solution and solid phase behaviour, including any possible relationship between them. Several analytical molecular techniques are adequate for this purpose, although vibrational spectroscopy is in a privileged situation. Raman spectroscopy is usually the technique of choice because it provides Raman shifts below 400 cm^{-1} from solids and aqueous solutions, also representing an advantage to study crystalline and amorphous structures. Nonetheless, the low intrinsic sensitivity of the conventional mode of operation of this technique represents a shortcoming.

Further, the use of computational chemistry to predict the Raman spectra of arsenic organic and inorganic compounds is of high interest. It would allow the exploration of new analyte identification procedures and give light to a better understanding of arsenic speciation in water solutions. In this matter, density functional theory (DFT) methods, which have a good performance for the prediction of vibrational frequencies and Raman intensities [7][8], have been successfully applied in Raman spectra calculations of arsenic-containing species [4][9][10]. However, most of these former measures have been performed in the gas phase considering neutral species. In principle, the progress in *ab initio* molecular dynamics methodologies may yield accurate predictions of vibrational spectra in solution, including anharmonic effects [12]. Unfortunately, these sophisticated methods are challenging to use and computationally very expensive, so that conventional DFT approaches are still the method of choice. Including explicit solvent effects in calculating IR and Raman spectra is a challenging problem [11]. Hence, further validation work comparing experimental and theoretical data is required to validate such DFT-based strategies that usually combine implicit and explicit descriptions of the solvent molecules.

This work aims to establish a relationship between the Raman spectra of the As oxoacids in aqueous solution at different pHs and the corresponding solid-phase precipitated. In addition,

we test a hybrid computational approach for the evaluation of the Raman shifts of the most relevant species of $As^{(III)}$ and $As^{(V)}$ oxoacids in an aqueous solution that couples a DFT representation of the oxoacid solutes and the closest water molecules to an implicit solvent model of the bulk solvent. We also propose potential analytical possibilities based on various theoretical developed approaches.

2. Experimental

2.1. Chemicals

We used chemicals of analytical reagent grade (Merck, Darmstadt, Germany). The sample solutions were prepared in distilled/deionised water (18 MΩcm). We used As_2O_3 and $NaAsO_2$ as models to study $As^{(III)}$ species, while As_2O_5 and Na_2HAsO_4 served as models for $As^{(V)}$ species.

2.2. Methods

Firstly, we alkalised all As solutions with NaOH (0.5 M) up to above pH ≈ 12.0 and then were progressively acidified by adding HCl (0.5 M) under continuous stirring to achieve successive precipitations. We generally selected the pH values according to the Eh-pH diagram to facilitate one predominant arsenic oxoacid at each pH. Thus, the nominal pH values were at 12.0, 9.5, 6.0, 3.0 and 0.5. The precipitated As oxoacids species were generated during the acidification process, recovering the precipitates formed at the selected nominal pHs. We adjusted the pH values just before recording the Raman spectra using a pH meter Mettler Toledo (Columbus, Ohio, USA) with a glass electrode.

2.3. Instrumentation

We obtained all Raman spectra by a BWTEK portable Raman spectrometer (Newark, DE, USA), *i*-Raman model, fitted with a refrigerated CCD detector, using the 785-nm line laser, CleanLaze model (300 mW) as the excitation source. The power level was set nominally at 100 % but reduced on several occasions due to the detector's saturation. The nominal experimental conditions were the following: 10 s accumulation time, 1 min acquisition time, 4 cm^{-1} spectral resolution, and spectral scanning range 150-3.300 cm^{-1}, whilst the results were processed using the Origin 9.0 software [Origin Lab Corporation, Northampton, MA, USA].

We recorded the Raman spectra of the As solutions in the backscattering geometry at room temperature. After adjusting and stabilising pH, we used golden plates as sample supports, putting on aliquots of 5 μL of the As aqueous solutions to increase the signal-to-background ratio of the recording Raman spectra. Getting well-resolved Raman bands from aqueous solutions is different due to the potential strong background scattering hydrogen bridges. We recorded the Raman spectra of the solid samples under the same experimental conditions. The nominal Raman shifts of the different As species were from the literature.

2.4. Computational studies

2.4.1. Preliminary validation calculations

We computed the vibrational frequencies of small arsenic compounds including AsClO, AsH_2F, AsH_3, $HOAsO_2$ and monomethylarsonic acid ($CH_3H_2AsO_2$; $MMA^{(III)}$) that present symmetrical and asymmetrical stretchings, scissors or symmetrical deformations. The experimental frequencies were obtained from the NIST Computational Chemistry Database [13] except for $MMA^{(III)}$, for which the work of Yang *et al.* was used [10]. We used several Kohn-Sham density functional theory (DFT) methods to calculate *in vacuo* the equilibrium geometries and harmonic frequencies employing the *Gaussian16* package [14]. In particular,

we considered the hybrid functionals B3LYP [15,16], PBE1PBE [17] and WB97XD [18,19] combined with Dunning´s double or triple-ζ basis sets augmented with diffuse functions [20–22]. We used both full-electron basis sets (denoted here as CVXZ with X=D, T) and variants including pseudopotentials (CVXZ-PP) for the As atom. Consequently, we tested twelve levels of theory, which have been satisfactorily used in arsenic systems by other authors [10,23]: B3LYP/CVDZ, B3LYP/CVDZ-PP, PBE1PBE/CVDZ, PBE1PBE/CVDZ-PP, WB97XD/CVDZ, WB97XD/CVDZ-PP, B3LYP/CVTZ, B3LYP/CVTZ-PP, PBE1PBE/CVTZ, PBE1PBE/CVTZ-PP, WB97XD/CVTZ and WB97XD/CVTZ-PP.

The Supporting Information (Tables S1-S2) reports the calculated harmonic frequencies and their relative errors *vs* the experimental data. We found that the B3LYP method yields the most accurate harmonic frequencies for all the compounds followed by PBE1PBE and WB97XD, resulting in global average errors of 2.1% (B3LYP), 3.7% (PBE1PBE) and 4.6% (WB97XD) using the CVTZ basis set (Tables S3-S4). Curiously, the inclusion of pseudopotentials (CVTZ-PP) improves the performance of the PBE1PBE (3.3%) and WB97XD (4.2%) methods, but it slightly deteriorates that of B3LYP (2.3%). The harmonic frequencies calculated with the double-ζ CVDZ basis set have lower errors in the case of PBE1PBE (3.1%) and WB97XD (3.7%), and a very similar error percentage in B3LYP (2.2%). However, the method and the basis set effects depend on the examined compound. For $MMA^{(III)}$, which is a particularly relevant test compound, the global error of the harmonic frequencies is 0.8% (B3LYP/CVTZ) and 2.0% (B3LYP/CVDZ).

Scaling factors (*f*) for obtaining fundamental vibrational frequencies from harmonic B3LYP frequencies derived using a least-squares approach. We required two scaling factors for frequencies below and above 900 cm^{-1} for a satisfactory correction. Application of the resulting scaling factors, $f_{<900}$=1.0103 / $f_{>900}$=0.9749 at B3LYP/CVTZ and $f_{<900}$=1.0240 / $f_{>900}$=0.9826 at B3LYP/CVDZ, improves the agreement between theoretical and experimental data for the

majority of the vibrational frequencies of the reference compounds, reducing the deviations to 0.5-1.5 %. These scaling factors can tentatively apply to other inorganic and organoarsenic compounds.

2.4.2. Raman spectra of $As^{(V)}/As^{(III)}$ oxoacids

We optimise the molecular geometries of the tetrahedral $As^{(V)}$ and trigonal-pyramid $As^{(III)}$ oxoacids at the B3LYP/CVTZ and B3LYP/CVDZ levels of theory [16,20,24] combined with the Polarisable Continuum Model (PCM) in the integral equation formalism (IEF) [25,26] and modelling the solvent as a continuum and isotropic dielectric medium characterised by the dielectric constant. The solute, described through its electronic density, embeds into a molecular-shaped cavity. We solve the electrostatic problem of the mutual polarisation of the solute and the continuum by applying boundary conditions at the solute/solvent interface, leading to the integral PCM equations. Similarly, we achieve the smooth solution of these equations by the continuous surface charge approach [27], fundamental for introducing solvent effects on energies and molecular properties. The calculation of the Hessian matrix of force constants was for all the optimised systems to confirm their character as true minima on the potential energy surface and obtain the harmonic vibrational frequencies. The Raman intensity calculation was within the PCM framework [28], including only equilibrium solvent effects on the harmonic frequencies. We performed all the quantum mechanical (QM) calculations with *Gaussian16* [14].

2.4.3. Raman spectra of $As^{(V)}/As^{(III)}\cdots(H_2O)_n$ Cluster Models

We employed a hybrid solvent model that includes explicit water molecules in the first hydration shell around the solute atoms to describe specific solvent effects on the harmonic frequencies and Raman activities. Thus, the clusters result embedded within the solvent continuum. Texting of the structure and flexibility of the hydration shells in aqueous solution

was by carrying out a preliminary molecular dynamics (MD) simulation of the arsenicals in an explicit solvent that provided thermalised structures, retrieving from which the cluster models.

The initial structures of the MD simulations were from the PCM-B3LYP/CVTZ optimised geometries of $As^{(V)}$ and $As^{(III)}$ species, solvated by a 25 Å spherical cap of TIP3P [29] water molecules centred at the As atom. We used the antechamber program using the GAFF force field [30][31] to assign molecular mechanics parameters for the solute species. We selected the bonded parameters to treat the As atoms from those available for phosphorous, while the vdW parameters were from the universal force field. Using the RESP methodology, the atomic charges for all the solute atoms were from the B3LYP/aug-cc-pVTZ electrostatic potential.

We carried out the hydrated systems' energy minimisation and MD calculations using the SANDER program included in the AMBER18 package [32,33]. We initially relaxed the water molecules using 1000 conjugate-gradient steps. Subsequently, we computed a 400 ps MD trajectory, only allowing the cap water molecules to move and further restraining the solvent cap at the 25 Å boundary by a harmonic potential with a force constant of 0.125 kcal/(mol $Å^2$). The time step of the MD simulations was 1.0 fs, and the SHAKE algorithm constrained all the bond lengths at their equilibrium values. A non-bond pair-list cut off of 15.0 Å was used, maintaining the temperature at 300 K using Berendesen's algorithm.

The MD simulations sampled the hydration shells of the $As^{(V)}$/$As^{(III)}$ species. Hence, we extracted one hundred equally-spaced MD snapshots from each trajectory to perform QM calculations on the cluster models, including the solute atoms and nearby water molecules. In particular, we selected the two closest water molecules around each solute atom, which resulted in clusters containing a varying number of water molecules (~7-8), given that some waters can bridge two or more solute atoms. All the cluster models relaxed at the PCM-B3LYP/CVDZ level of theory, followed by harmonic frequency calculations and Raman scattering activity

calculations. We note that this approach is computationally expensive as the geometry optimisations of the cluster structures converge slowly (*e.g.*, around 12 h of wall time per structure running on a 12-core server).

We used the Multiwfn program [34] to transform the Gaussian output files into theoretical spectra convoluting peak intensities with a Lorentzian function, with a full width at half maximum (FWHM) of 4 cm^{-1}. We averaged the resulting cluster spectra to obtain the final Raman spectrum of each $As^{(V)}/As^{(III)}$ species. Using the MOLDEN program, we visualised different vibrational modes in a representative sample of cluster models to help assign the theoretical Raman spectra.

2.4.4. Arsenic speciation calculations

For the sake of comparison with the experimental results at each selected pH, we used theoretical Raman spectra averaging the computational spectra of the individual As oxoacids species according to their fractional concentrations regulated by the pK_a values.

3. Results and discussion

As stated above, the molecular geometry of the arsenic oxoacids in aqueous solutions is assumed to be pyramidal for $As^{(III)}$ with a stereochemically active lone pair and tetrahedral for $As^{(V)}$, both structures showing different site (point group) symmetry depending on the protonation degree (Table S5). The theoretical molecular symmetry allows us to use the Raman bands of the As=O and As–OH vibrations to characterise the oxygenated inorganic $As^{(III)}$ and $As^{(V)}$. The corresponding two symmetric bands relate to the bonds belonging to the non-bridging and bridging oxygen atoms. The wavenumber of the bridging oxygen atoms usually falls in a lower region, while the relative intensity of both bands depends on the non-bridging-to-bridging oxygen ratio. In any case, not all theoretical bands are visible in the Raman spectra

due to several reasons, including the low intrinsic sensitivity of the Raman spectrometry, band overlapping, and the existence of degenerated levels, among others.

We obtained the Raman spectra of the different $As^{(III)}$ and $As^{(V)}$ oxoacids in solution at different pH values, according to the Eh-pH diagram and the fractional distribution of the distinct $As^{(V)}$ and $As^{(III)}$ oxoacids species with pH (Fig. S1). We use the pK_a values theoretically deduced from the internal energy, ΔE, of the different $As^{(III)}$ and $As^{(V)}$ oxoacids [35] to build Fig. S1 according to the following developed theoretical equations,

$$pK_a = (147.174 \pm 2.735) \cdot \Delta E\left(As^{(V)}\right) - (64.153 \pm 1.322)\,; \quad R^2 = 0.999 \qquad (1)$$

$$pK_a = (70.926 \pm 8.935) \cdot \Delta E\left(As^{(III)}\right) - (24.312 \pm 4.528)\,; \quad R^2 = 0.984 \qquad (2)$$

The pKa values from Eq. (1) and Eq. (2) agree well with those found in the literature. We selected different pH values to acquire the Raman spectra, but from some of them, several arsenic species coexist, deforming the shape and shifting the maximum of the Raman peaks. Nonetheless, as an advantage, information from these complex situations usually supports or help in clarifying the conclusions derived from other pHs.

3.1. Effect of pH on arsenic speciation

3.1.1. $As^{(V)}$ species

The Raman spectra of the $As^{(V)}$ aqueous solutions, prepared from $Na_2AsO_3(OH)$ and As_2O_5, show similar patterns at any pH (Fig. 1 A, B, and Table 1). Under very alkaline conditions (pH ~12.0), AsO_4^{3-} is the predominant $As^{(V)}$ oxygenated species (~75%), although coexisting with fewer amounts of $AsO_3(OH)^{2-}$ (~25%). At these high pHs, the Raman spectra of the $As^{(V)}$ solutions show mainly the contribution from AsO_4^{3-} species. The group theory

considers T_d symmetry for AsO_4^{3-} and four distinct Raman active molecular vibrational modes (Table S5), which appear in two vibrational regions (Fig. 1A). The lower (deformation) region shows one peak ν_4 about 408 (F_2 out-of-plane bending mode, δ_{as}) and a second one ν_2 at 350 cm^{-1} (doubly degenerate *E*, δ_s) (As–O symmetric bending of AsO_4^{3-}). The higher wavenumbers region exhibits a peak ν_1 at 815 cm^{-1} (non-degenerate A_1 symmetric stretch) overlapping strongly with a minimal shoulder ν_3 at 786sh cm^{-1} (triply degenerate F_2 asymmetric) of As–O stretching vibrations. Furthermore, some lattice modes between 100 and 250 cm^{-1} are also present.

The precipitated phase obtained at pH ~12.0 would be Na_3AsO_4, which crystallises in the space group $P\bar{3}_{cl}$. It shows four fundamentals internal vibrations (Fig. 2 A, B, and Table 2) above 500 cm^{-1}, according to a tetrahedral AsO_4^{3-} ion with T_d symmetry. Only the peak at 822 cm^{-1} agrees well with that obtained from the aqueous solution (815 cm^{-1}). The other three bands at 1065↓, 790sh and 770sh cm^{-1} characterise the dry solid-phase generated from $Na_2AsO_3(OH)$ solutions. Working with As_2O_5, only the peak at 789sh cm^{-1} (ν_{as} As–O) is additionally present. These differences in the Raman spectra of both solutes might result from the less sodium present working with As_2O_5, which facilitates forming an oxygen-deficient sodium arsenate with a tentative molecular formula $Na_7As_{11}O_{31}$ trigonal, space group $P\bar{3}_{ml}$ [36]. Nonetheless, some authors [37] reported Raman bands similar to those found in this work (Table 1) for the solid $Na_2AsO_3(OH)\cdot 7H_2O$, although depending on the precipitation conditions, other possible, solid species, such as $Na_4(AsO_4)OH$, which crystallise in the orthorhombic space group P_{nma}, could also be formed [38].

The tetrahedral unit of AsO_4^{3-} changes to lower symmetries if protonated or joined to metals, splitting the degenerate vibrations and shifting the stretching vibrations. At pH 9.5, $AsO_3(OH)^{2-}$ with a C_{3v} molecular symmetry becomes predominant (~99%) in solution. The

hydroxyl group gives rise to three fundamental frequencies, stretching and bending (in-plane and out-of-plane). On the other hand, the As-O stretching theoretically should show three possible bands, according to the C_{3v} symmetry. However, the experimental Raman spectra only exhibit two bands at 700 and 838 cm^{-1}, related to the symmetric A_1 vibrations of the As–OH and As–O groups, respectively. The As–O bond of $AsO_3(OH)^{2-}$ has a theoretical double bond character against the As–OH single bond (Fig. 1A). Nonetheless, both bonds show fractional bond orders, with a stretching force greater for As–O than for As–OH. In the lower wavenumber region (500-200 cm^{-1}), three O–As–O deformation modes are possible from C_{3v} symmetry, but the Raman spectra only show two bands at 326-334 and 386-393 cm^{-1}.

The precipitated phase formed at pH 9.5, $Na_2AsO_3(OH)$, crystallises in the space group P_{21}/n with four formula units per unit cell. The $As^{(V)}$ atoms occupy "general positions", and consequently, the $AsO_3(OH)^{2-}$ anion has C_{3v} site symmetry. The fundamental vibrations of the solid compound $Na_2AsO_3(OH)$ are non-degenerate and Raman active. Three bands at 840, 808, and 740 cm^{-1} are visible in the As–O stretching region (Fig. 2). The peak at 840 cm^{-1} agrees well with that found in the solution. However, the band at 740 cm^{-1}, ascribed to As–OH stretching, suffers hypsochromic effect, blue-shifting 40 cm^{-1} from the corresponding frequency at 700 cm^{-1} in the solution spectrum. Participation of the OH groups in strong hydrogen bridges derives from the presence of the Raman band at 808 cm^{-1}, only visible for the solid phase, which probably arises from a highly symmetric vibration of polymeric species. The solid phase also shows five frequencies in the deformation region at 420sh, 402, 378, 344 and 318 cm^{-1}. The bands at 318 and 344 cm^{-1} assign to symmetrical AsO_3 deformations and AsO_3 rocking, while the Raman band at 378 cm^{-1} ascribes to asymmetrical AsO_3 deformation. The other two bands from the solid phase probably give rise to only one peak in the Raman spectrum of the aqueous solution due to the broadening and overlapping of the peaks. Further, two Raman shifts at 180 and 140 cm^{-1} due to lattice vibrations appeared for the solid phase.

304 At neutral pHs (~7.0), a nearly equimolecular (~50%) mixture of $AsO_3(OH)^{2-}$ and
305 $AsO_2(OH)_2^-$ exists in an aqueous solution (Fig. S1A), where the $AsO_2(OH)_2^-$ species shows a
306 C_{2v} molecular symmetry. Group theory offers four stretching modes and five deformational
307 modes for this symmetry. However, the experimental Raman spectra obtained at pH 6-7 only
308 show four bands at 700 cm^{-1} (A_1, ν_s $As(OH)_2$), 842 cm^{-1} (A_1, ν_s AsO_2), 745 cm^{-1} (B_1, ν_{as} As–
309 OH) and 870sh cm^{-1} (B_2, ν_{as} As–O), which agree with the valence bond structure of this anion.
310 However, working with the solute As_2O_5, the shoulder at 870 cm^{-1} disappeared. The Raman
311 spectra from solutions of both solutes also show peaks at 380 and 345 cm^{-1} and 325 cm^{-1} from
312 As_2O_5.

313 The precipitate formed at this pH would be a $NaAsO_2(OH)_2$ and $Na_2AsO_3(OH)$ mixture.
314 The solid $NaAsO_2(OH)_2$ consists of two sodium cations and tetrahedral $(HO)_2AsO_2^-$ anions.
315 Distorted octahedral coordination spheres define the asymmetric unit, where six O atoms of
316 five $AsO_2(OH)_2^-$ groups surround each sodium cation [39]. The Raman spectra of crystalline
317 $NaAsO_2(OH)_2$ differ slightly from the aqueous solution. The Raman bands appeared in the As–
318 O stretching region at 721, 808, 840, 870 and 905sh cm^{-1} for $Na_2AsO_3(OH)$ and 774-789 and
319 905sh cm^{-1} for As_2O_5 (Fig. 2). The weak shoulder at 905-911 cm^{-1} corresponds to the As–O
320 bond's symmetric vibration (A_1). The two bands at 840 and 870 cm^{-1} of the solid $Na_2AsO_3(OH)$
321 agree with the aqueous solution, while none from for As_2O_5. Assuming free $AsO_2(OH)_2^-$
322 groupings in the crystal, two As–O stretchings and two As-OH stretchings can appear, but with
323 different intensities. One of the As–O bonds probably forms a strong hydrogen bridge with a
324 hydroxyl from a different $AsO_2(OH)_2^-$ group or a water molecule, shifting its frequency to
325 lower values. Four bands were observed in the deformation region for the solid phase at 340,
326 380, 402sh and 433sh cm^{-1} for $Na_2AsO_3(OH)$ and 303, 343, 385 and 432 cm^{-1} for As_2O_5.

327 Under more acidic aqueous conditions (pH 3.0), $AsO_2(OH)_2^-$ predominates (~85%)
328 together with small amounts (~15%) of $AsO(OH)_3$ (C_{3v} symmetry). Group theory shows six

fundamental skeletal vibrations (three stretching modes A_1 and three deformation modes E) for $AsO(OH)_3$. Thus, the Raman spectra may exhibit normal modes similarly to the $AsO_2(OH)_2^-$ system (predominating species) but red-shifted. Fig. 1 (A, B) shows a strong band at ~745 cm^{-1} for As_2O_5 and Na_2AsO_3OH solutions, corresponding to the As–OH symmetric stretch (A_1). The Raman band at 877 cm^{-1} relates to ν_1 (A_1) of $AsO_2(OH)_2^-$. In the region 200-500 cm^{-1}, two deformation modes usually appeared, but only one band at 367 cm^{-1} exists, which correlates with the F_2 deformation mode of the AsO_4^{3-} ion.

The solid phase shows peaks at 910, 789, 774 cm^{-1} from $Na_2AsO_3(OH)$ solutions and 910, 850sh, 833, 809, and 740 cm^{-1} from As_2O_5 solutions (Fig. 2), similarly to pH 7.0. The peak at 774 cm^{-1} due to the As–OH groups' asymmetric (E) vibrations is absent if working with As_2O_5. It is worth noting that changing the pH value from 7.0 to 3.0, the peaks at 700 and 840 cm^{-1} disappear, generated from $AsO_3(OH)^{2-}$, whose content at pH 3.0 is residual. The peaks at 433-420sh, 380, 340, 320-302, 180, and 140-150 cm^{-1} were also present in the solid phase.

Increasing acidity (pH 0.5), the full protonated $As^{(V)}$ species $AsO(OH)_3$ becomes dominant (~98%), showing C_{3v} symmetry. The Raman spectra profile show an additional slightly red-shift, showing two peaks at 764 and 932 cm^{-1} (Fig. 1), which ascribe to the two A_1 vibrations, respectively assigned to the As–O stretching (predicted by the valence structures as a double bond) and the symmetrical As(OH) stretchings. Lowering the solution pH, the shoulder at 877 cm^{-1} from pH 3.0 suffers a blue shift up to 932 cm^{-1}. The lower region contains the peak at 345 cm^{-1} assigned to symmetrical deformation A_1 and rocking E of $As(OH)_3$. Furthermore, the tiny band at 270 cm^{-1} ascribes to the asymmetric E $As(OH)_3$ deformation does not appear in solution but the solid phase. In the region of the O–As–O deformations, 200-500 cm^{-1}, two narrow bands appeared at 304 and 364 cm^{-1} together with two broad bands at 260 cm^{-1} and 450 cm^{-1}. However, in the solid phase, additional bands also appeared at 932, 860-870

and 380-400 cm^{-1}. The solid arsenic acid $AsO(OH)_3$ appears as white crystals but changing the drying conditions, different hydrates, such as $As_2O_5 \cdot (5/3)H_2O$, $AsO(OH)_3 \cdot 2H_2O$, or the hemihydrate $AsO(OH)_3 \cdot (1/2)H_2O$, are also possible. The Raman peaks from both solutes are similar (Fig. 2).

3.1.2. $As^{(III)}$ species

According to the Eh-pH diagram, we considered the distinct $As^{(III)}$ oxoacid species with the speciation displayed in Fig. S1B. We also acquired the Raman spectra of the aqueous solutions containing either $NaAsO_2$ or As_2O_3 as solutes at different pHs (Fig. 3 A, B, Table 1). Among the distinct $As^{(III)}$ oxoacids, $As(OH)_3$ and $AsO(OH)_2^-$ show the highest interest in aqueous systems because they predominate under natural environmental conditions. The symmetry of the AsO_3^{3-} and $As(OH)_3$ species belong to the C_{3v} point group, showing two non-degenerate (A_1) and two doubly degenerated (E) vibration modes, all of them are Raman active, but the recorded Raman spectra only exhibit the stretching modes. On the other hand, the $AsO_2(OH)^{2-}$ and $AsO(OH)_2^-$ species results in a C_s symmetry, exhibiting three Raman bands owing to the stretching vibrations of two symmetric A' and one asymmetric A'' modes.

The AsO_3^{3-} oxoacid belongs to the C_{3v} point group, giving Raman bands at 790 cm^{-1} (As–O symmetric stretch), 580 cm^{-1} (asymmetric stretch), and often a bending mode 340-317 cm^{-1}. Under the experimental conditions used, the solutions of arsenic trioxide, As_2O_3, treated with sodium hydroxide produce mixtures of sodium *meta*-arsenite, $NaAsO_2$, and sodium *ortho*-arsenite, Na_3AsO_3. Sodium arsenite consists of a polymer backbone $[AsO_2]_n^{n-}$ with the connectivity –O–As(O^-)– associated with sodium cations. The free anion AsO_3^{3-} only predominates at very alkaline pH (pH > 14) (Fig. S1B), but lowering the pH up to ≈ 13.0, $AsO_2(OH)^{2-}$ with a C_s symmetry predominates (~65%) together with fewer levels of AsO_3^{3-} (~30%) and $AsO(OH)_2^-$ (~5%). However, we ignore this situation because the aqueous

solutions at such a high pH are of no interest due to their absence in the natural environment. For this reason, we start this section sampling at pH 12.0.

In aqueous solutions at pH 12, the anions $AsO(OH)_2^-$ (~52%) and $AsO_2(OH)^{2-}$ (~48%) coexist in approximately similar proportions (Fig. S1B). Nonetheless, other $As^{(III)}$ species, such as *m*-arsenite AsO_2^-, can probably also exist at this pH, although additional confirmation is still required. The Raman spectra of $As^{(III)}$ ($NaAsO_2$ and As_2O_3) solutions at pH 12.0 (Fig. 3 A, B) show two broad bands picking at 784-793 cm^{-1} (As–O symmetric stretch) and 575-586 cm^{-1} (As–O asymmetric stretch) (Table 1). The higher band is probably the result of an overlapping of the stretching vibrations of $AsO(OH)_2^-$ (784 cm^{-1}), $AsO_2(OH)^{2-}$ (770 cm^{-1}) and AsO_3^{3-} (750 cm^{-1}). The second band at 575-586 cm^{-1} is broad, being probably also the convolution of others. Working with the $NaAsO_2$ solution, the peak at 1065 cm^{-1} appeared even up to pH 10. This peak is probably due to the arsenodiester symmetrical stretching ν(O–As–O), or to the arsenodioxy symmetrical stretching $\nu(AsO_2^-)$ (Transverse vibrational modes), similarly as for phosphorous. The solid phases, $Na_2AsO_2(OH)$, generated at pH 12.0, show two prominent bands at 843 and 700 cm^{-1}, with a peak at 1070 cm^{-1} (Fig. 4, and Table 2). A shoulder at 785 cm^{-1} from the $NaAsO_2$ solution was also present in the Raman spectra of the wet solids (Fig. 4 A, B and Table 2). Several peaks between 566 and 108 cm^{-1}, mainly due to bending and lattice modes, also appeared in the low region.

At lower basic pHs (pH ≈ 10.5), $AsO(OH)_2^-$ predominates (~92%) in large extension in solution. It gives the Raman bands at 784 cm^{-1} (As–O stretch) and two others at 712 (As–OH asymmetric stretch) and 575 (As–OH symmetric stretch) cm^{-1}. $AsO(OH)_2^-$ belongs to C_s symmetry with a mirror plane, giving six theoretical Raman shifts. However, only one of the three possible bending modes appeared at 317 cm^{-1}. Notwithstanding, the peak at 1065 cm^{-1}

400 appeared from the alkaline aqueous solutions of $NaAsO_2$ (pH ≥ 10.5) (Fig. 3, and Table 1) and
401 the solid phases (Fig. 4, and Table 2) of $NaAsO_2$ and As_2O_3.

402 Following acidification, we can note the contribution of $As(OH)_3$ in the Raman spectra.
403 Thus, the Raman spectra at pH ~9.0, $AsO(OH)_2^-$ (~65%) and $As(OH)_3$, (~35%) (Fig. 3 A, B)
404 show two broad bands peaking at 791-784 and 712-700 cm^{-1}, which may assign to A'' and A'
405 As–O stretching vibrations. Further, the expected modes of C_s symmetry include bands at 535
406 and 585-651 cm^{-1}, related to the A' stretching vibration of As–OH. Also, the peaks at 340 and
407 317 cm^{-1} appeared from As_2O_3 and $NaAsO_2$ solutions, respectively. Decreasing the pH from
408 10.5 to 9.5, the Raman peak at 1065 cm^{-1} disappears, while another peak appears at 651 cm^{-1}
409 working with $NaAsO_2$. The solid species formed at pH 9.5 show slightly different Raman
410 spectra from As_2O_3 and $NaAsO_2$ solutions (Fig. 4). The dry solid of $NaAsO_2$ provides Raman
411 spectra with only two peaks at 785 and 566 cm^{-1} and four additional peaks in the lower region
412 (Fig. 4, and Table 2). Contrarily, the dry solid of As_2O_3 generate Raman peaks at 828, 750, 643
413 and 560 cm^{-1}, together with 12 additional peaks in the lower region (Fig. 4, and Table 2),
414 probably due to the differences existing in the amount of the sodium ions present, which can
415 generate different stoichiometric salts.

416 At neutral and acidic pHs, the only predominant species in solution is arsenous acid,
417 $As(OH)_3$ (>99%), which is the essential arsenic species from an environmental point of view
418 [40]. The Raman spectra of the $As^{(III)}$ solutions at acidic pHs (Fig. 3 A, B, and Table 1) exhibit
419 a distinctive band at about 700 cm^{-1} (A_1) tailing to lower frequencies (650sh cm^{-1}) (E) assigned
420 respectively to the As–OH symmetric and asymmetric stretchings. An additional peak at 408
421 cm^{-1} appears from $NaAsO_2$ solutions. One tautomer of arsenous acid is arsonic acid,
422 $HAsO(OH)_2$. However, it has not been isolated or well-characterised yet in solution.
423 Nonetheless, under high concentrations of hydrochloric acid (very acidic solutions), other

$As^{(III)}$-oxohydroxy species, such as $As(OH)_2Cl$, $As(OH)Cl_2$, $As(OH)_2^+$, $AsCl_3$, AsO^+, $HAsO_2$ and AsO_2^-, can coexist in equilibrium. Nonetheless, the contribution of these $As^{(III)}$ species to the Raman spectra would be minimal because no differences exist in the Raman spectra at any lower pH. Further, in many situations, the formation of some of them requires the simultaneous presence of a favourable redox process [41][42][43][44]. In any case, definitive experimental evidence is still lacking. The solid phases obtained at neutral and acidic pHs also provide similar Raman spectra patterns with peaks different to those reported from the solution (Fig. 4, and Table 2). In the high shifts region, the Raman band at 779-785 cm^{-1} is typical, together with several minor peaks in the deformation region (Fig. 4 (A, B) and Table 2), some of them slightly shifted concerning those reported for As_2O_3 nanofilms [45][46], although the last ones obtained by SERS [46][47].

As a general conclusion from this section, we can state that the Raman spectra of the dry precipitates generated from $NaAsO_2$ and As_2O_3 solutions (Fig. 4 A, B) differ very strongly between them and with the Raman spectra from aqueous solutions. We noted essential differences in the Raman spectra of the dried $As^{(III)}$ precipitated from $NaAsO_2$ and As_2O_3 solutions, particularly at pHs below 9.5 (Fig. 4 A, B), showing a very complex pattern in the whole Raman region covered (Fig. 4 A, B). Notwithstanding, below pH 5.0, the Raman spectra of the solid formed from the solutions of $NaAsO_2$ show strong fluorescence.

3.2. Computational studies

3.2.1. Theoretical Raman spectra of the individual $As^{(V)}$/$As^{(III)}$ oxoacids

For the frequency range of interest, 200-1000 cm^{-1}, the theoretical Raman spectra of the $As^{(V)}$ molecules within the continuum solvent consist of ~3-4 peaks that are unambiguously assigned to symmetrical or asymmetrical stretching motions of the As–O or As–OH moieties (Fig. S2). The stretching of the As-OH bonds also presents a minor coupling with As-O-H

rocking (bending) motions. Ongoing from H_3AsO_4 to AsO_4^{3-}, most active As–O peaks red-shift gradually from 953 to 764 cm^{-1} and the As–OH vibrations from 707 to 554 cm^{-1}. The symmetrical stretching peaks of various As–O or As-OH bonds are two- or three-fold more intense than the asymmetrical ones. When comparing the CVTZ and CVDZ spectra of the oxoacids, we found that the double-ζ calculations systematically underestimate the vibrational frequencies by 1-2% (Fig. S2) for the triple-ζ results, especially for the tetrahedral $As^{(V)}$ species. This basis set effect is uncorrected by applying the scaling factors derived from the small molecule set ($f_{<900}$ and $f_{>900}$). Considering that the more flexible CVTZ basis set generally provides a better description of molecular properties and that the $As^{(V)}/As^{(III)}$ oxoacids are highly polar and charged species, we obtained *specific* scaling factors for each oxoacid molecule to improve the agreement between the CVTZ and CVDZ frequencies. We approximate the experimental data by applying such scaling factors to the theoretical spectra of the water-oxoacid cluster models (see below), computed at the PCM-B3LYP/CVDZ for computational reasons.

Indeed, the electrostatic effects introduced by the solvent continuum are not enough to calculate realistic Raman spectra in aqueous solution for the $As^{(V)}/As^{(III)}$ oxoacids because the PCM method cannot account for the *specific* H-bonds between the solute and solvent. Therefore, we included direct solvent effects using static DFT calculations on cluster models comprising the solute molecule and the nearby waters. We considered 100 clusters whose initial geometries were extracted from classical MD simulations and subsequently fully relaxed at each oxoacid species PCM-B3LYP/CVDZ level. However, we noted that during the geometry optimisations, some water molecules are reoriented concerning their location in the MD frames to maximise their H-bond interactions with the solute O atoms or other waters (*i.e.*, no direct $As\cdots(H_2O)$ contact are formed in the $As^{(III)}$). A visual inspection of the optimised structures confirmed that the solute O atoms form H-bonds with ~1-3 water molecules and exhibit variable

H-bonding patterns (see examples in Fig. S3). Thus, we expect that the cluster ensembles could describe the most critical effects of short-range solute-solvent interactions.

As expected, the peaks associated with stretching the As–O and As–OH moieties in the continuum solvent PCM split into several signals, shift in frequency, and show attenuated Raman activities (see examples in Fig. S3). We analysed in detail the peak assignments of several cluster models for each oxoacid species (Tables S6-S7) and found a very significant coupling between the solute and solvent coordinates in the most active normal modes that also perturb direct H-bond contacts. The percentage weight of water coordinates in the vibrational modes involving the oxoacid solutes is highly variable, ranging from ~5% to ~90%. The average percentage in the examined systems are 23, 48, 59 and 54 % for H_3AsO_4, $H_2AsO_4^-$, $HAsO_4^{2-}$ and AsO_4^{3-}, respectively, and 49 and 56% for H_3AsO_3 and $H_2AsO_3^-$. The solute-solvent coupling is more critical in those normal vibration modes involving As-OH stretching and As–O–H rocking motions than in the As–O stretching. This coupling is particularly notorious in H_3AsO_3 and $H_2AsO_3^-$ spectra, where the As–OH peaks appear more widely dispersed owing to the H-bond effects. Overall, the analysis of the few cluster structures and Raman spectra reveals the magnitude and variability of the solute-solvent coupling, thus indicating the necessity of conformational sampling.

3.2.2. Theoretical Raman spectra of the pH-averaged $As^{(V)}$/$As^{(III)}$ oxoacids

The pH-averaged theoretical spectra, which admit a direct comparison with the experimental data (Fig. 1B for $As^{(V)}$ and 3B for $As^{(III)}$), are displayed in Fig. 5 (A, B) for the $As^{(V)}$ and $As^{(III)}$ species. We note a reasonable agreement between the calculated and experimental spectra, with minor differences in the Raman frequency, relative intensity and band shape.

Nevertheless, the $As^{(V)}$ spectrum recorded at pH=11.9 closes the theoretical one, which is a mixture of the tri-anion AsO_4^{3-} (69% concentration) and $HAsO_4^{2-}$ (31%) and exhibits the main band at 795 cm^{-1}, around 20 cm^{-1} below the experimental one (815 cm^{-1}). However, the position of the smaller band at 411 cm^{-1} is in good agreement with the observed experimentally (410 cm^{-1}).

At pH=9.6, the theoretical calculation predicts domination of $HAsO_4^{2-}$ (98%), reporting multiple As–O small bands overlapping within the 750-900 cm^{-1} range. Despite the residual noise in this calculated band, its positioning and shape compare favourably with the skewed shape of the experimental As–O band at 838 cm^{-1}. Ongoing the comparison, there are some discrepancies in the small band's position around 700 cm^{-1} (experimental) and 614 cm^{-1} (theoretical), most likely assigned to As–OH vibrations strongly coupled with solvent molecules. However, the band at 381 cm^{-1} is again around 20 cm^{-1} red-shifted from the experimental (400 cm^{-1}).

At neutral pH (6-7), the experimental Raman spectra display smaller and skewer As–O bands between 800 and 900 cm^{-1}, together with weak and noisy signals between 700 and 750 cm^{-1} for As–OH vibrations and a more specific band around 380 cm^{-1}. These three features are reproduced well by the theoretical spectra arising from an $H_2AsO_4^-$ (90%) - $HAsO_4^{2-}$ (10%) mixture that exhibits a noisy and wide As–OH band around 721 cm^{-1} and several overlapped As–O bands between 800 and 900 cm^{-1}. The As–O band shape is quite similar in the theoretical and experimental spectra. The theoretical calculations show a band around 380 cm^{-1} in agreement with the experimental data at lower positions.

When the solution becomes very acidic, pH=2.1, it contains more similar fractional concentrations for H_3AsO_4 (59%) and $H_2AsO_4^-$ (41%), and the relative intensities of the As–OH and As–O bands are also similar thanks to the enhanced Raman activity of the symmetric stretching of the three As–OH bonds in H_3AsO_4. The As–O and As–OH theoretical bands

coincide with the experimental spectra, 700-800 cm^{-1} (As–OH) and 820-900 cm^{-1} (As–O). For the latter vibrations, the calculation discriminates well between the single As–O stretching of H_3AsO_4, giving a small band at 917 cm^{-1} and the As–O stretchings motions of $H_2AsO_4^-$ at 876 cm^{-1}. We noted a single band experimentally, although it shows a shoulder at 900 cm^{-1} corresponding to H_3AsO_4.

In strongly acidic solutions, pH=0.5, the arsenic acid would be the dominant species (98%), and the intensity of the As–OH and As–O bands reversed in both the theoretical and experimental data. However, the band maxima are slightly different at 735 cm^{-1} and 917 cm^{-1} (theoretical) *vs* 764 cm^{-1} and 932 cm^{-1} (experimental), while the wideband at 340 cm^{-1} is very close to the experimental (345 cm^{-1}).

On the other hand, concerning the $As^{(III)}$ species in solution, Fig. 5B shows the low Raman activity/intensity of the $As^{(III)}$ spectra as compared with those of the $As^{(V)}$ species. At very alkaline pH (11.2), the $H_2AsO_3^-$ anion produced a wide As-OH band (500-650 cm^{-1}), while the As–O stretching activity is between 650 and 850 cm^{-1}. The two bands are well outlined in the theoretical spectra and are close to the experimental data frequencies: 586 cm^{-1} and 811 cm^{-1} (theoretical) *vs* 586 cm^{-1} and 793 cm^{-1} (experimental). The band around 391 cm^{-1} does not agree with the experimentally noted (340 cm^{-1}) at lower frequencies. This shift difference and the different shape are probably due to the more critical solute-solvent coupling in the normal vibration modes involving As–OH stretching and As–O-H rocking motions than those presenting As–O stretchings as observed for $As^{(V)}$ spectra.

Lowering the pH value to 8.9, 65% of the weak arsenic acid coexists with 35% arsenate. Under this situation, the feeble Raman activity generates the As–OH symmetrical stretching band at 693 cm^{-1} (theoretical) – 700 cm^{-1} (experimental) and an even smaller As–O band at 809 cm^{-1} (theoretical), partially visible in the experimental spectrum at 794 cm^{-1}. Similarly, at acidic pHs (below 6.0), where the only $As^{(III)}$ species is the arsenious acid, the theory predicts the As–

OH band a left-skewed extended between 600 and 750 cm^{-1} as experimentally observed, improving the agreement between theory and measurements.

3.3. Discussion

The Raman spectra of the $As^{(V)}$ and $As^{(III)}$ oxoacids in aqueous solutions change with pH according to their structural geometry (symmetry). The Raman bands of the $As^{(III)}$ oxoacids in solution suffer a more intense broadening than the $As^{(V)}$ oxoacids. This behaviour responds to the pyramidal structure of the $As^{(III)}$ oxoacids, enabling hydration of their As–O and As–OH groups, according to the minor average per-molecule water binding energy stated for the $As^{(III)}$ species [48]. To enhance the assessment of the water and the $As^{(V)}$ or $As^{(III)}$ oxoacids interaction, Tables S6 and S7 show the computed H_2O weigh in the motions for different frequencies in some representative *solute*$\cdots(H_2O)_n$ clusters. In the set of the examined clusters, the average H_2O weight is 23.0% (H_3AsO_4) *vs* 48.9% (H_3AsO_3), resulting in broader peaks (bands) in H_3AsO_3 than in H_3AsO_4. A closer inspection of the individual theoretical spectra of the individual $As^{(V)}$ and $As^{(III)}$ oxoacids shown in Fig. S3 allows us to obtain the same conclusion. A similar pattern can be observed for other $As^{(V)}$ and $As^{(III)}$ oxoacids pairs in this work. We note in passing that the visualisation of the moieties of some representative clusters allows us to confirm the formation of hydrogen bonds that, together with various $As^{(III)}$ oxoacids under the same alkaline pH conditions, could contribute to the peak overlapping. The As–OH vibrations occur at more downward Raman shifts than the As–O vibrations for $As^{(V)}$ species in solution and solid phase (Tables 1, 2), probably a result of the shorter and stronger As–O bonds (bond order ≤ 2) than of As–OH bonds (bond order ≥ 1) (Fig. S2) [37][49][50]. We can view this protonation-based red-shift by comparing the Raman spectra obtained at basic (9.5) and acidic (0.5) pHs, where $As^{(V)}$ shows the exact site symmetry (C_{3v}). However, the contrary occurs

569 for As(^{III}) species in solution (Table 1) and solid phase (Table 2), although into a shorter
570 wavelength region.

571 The Raman shifts in the region 700-900 cm^{-1} of $As^{(V)}$ solutions decrease with pH, but
572 the contrary occurs with the Raman peak at 400 cm^{-1}. The Raman shifts of the $As^{(V)}$ oxoacids
573 as a function of pH fit well a straight line that identifies the possible $As^{(V)}$ species present. Thus,
574 for the As–O (~900 cm^{-1}) and As–OH (~800 cm^{-1}) bonds of As_2O_5 and Na_2HAsO_4 solution, we
575 derived the two following equations,

576 $$\text{Raman shift}_{(\sim 900\ cm^{-1})} = (919.7\pm12.0) + (-9.2\pm1.5)\ [pH] \qquad (R^2 = 0.99825) \qquad (3)$$

577 $$\text{Raman shift}_{(\sim 800\ cm^{-1})} = (766.1\pm4.0) + (-7.3\pm0.6)\ [pH] \qquad (R^2 = 0.99282) \qquad (4)$$

578 for a pH range between 0.5 and 12.0. The slopes of the straight lines for other conditions are in
579 Table S8.

580 Alternative possibilities arise using intensity ratios from the Raman spectra of $As^{(III)}$
581 solutions. The I_{700}/I_{900} ratio grows for smaller pHs, which means that the peak in the region 700
582 cm^{-1} increases faster than in the region 900 cm^{-1}, resulting in the slope of the trend related to
583 the region of 900 cm^{-1} is smaller. Alternatively, exponential decay equations were possible for
584 As_2O_5 and Na_2HAsO_4 using the 764/932 ratio as a function of pH,

585 $$\text{Intensity}_{(764/932)} = (0.0\pm0.0) + (5.9\pm0.1)\ \text{Exp}([pH]/(1.8\pm0.1)) \ (R^2 = 0.99953) \qquad (5)$$

586 With the rate constant $k = 0.6\pm0.0$ cm^{-1} and the time constant $\tau = 1.2\pm0.0$ cm, for pHs in the
587 range between 0.5 and 12.0.

588 A comparison of the experimental and theoretical Raman spectra of $As^{(III)}$ and $As^{(V)}$ in
589 aqueous solutions shows that the $As^{(III)}$–O vibrations occur at lower frequencies than the $As^{(V)}$–

O vibrations, suggesting that the $As^{(III)}$–O bond is weaker than that of $As^{(V)}$–O, which correlates well with their calculated bond orders (Fig. S2). Using the so-called delocalisation index as a measure of the bond order [51], we found an exponential decay equation between the bond length (BL) and the bond order (BO) for the $As^{(III)}$–O and $As^{(V)}$–O bonds, as stated before for C–C, C–O and C–H bonds [52],

$$(BL) = (1.6\pm0.0) + (12.1\pm2.0)\exp\{(-BO)/(0.2\pm0.0)\} \qquad (R^2 = 0.99731) \qquad (6)$$

with the rate constant $k = 5.1\pm0.3$ cm^{-1} and the time constant $\tau = 0.1\pm0.0$ cm.

The Raman spectra of the $As^{(V)}$ and $As^{(III)}$ aqueous solutions at low concentrations show similar patterns to those found under saturation conditions. Dilution leads to changes in the intensity of the Raman peaks but not in the peak shifts. These results suggest that As species in solution undergo minor quantitative structural changes with dilution, only some hydrogen bridge alterations could happen. These results disagree with those reported in other works [53][54][55], probably owing to differences in the concentration range and the instrumental conditions used. The results from this work mean that pH plays a major criterion for evaluating stability and speciation of the As oxoacids in solution, while As concentration shows a quantitatively minor role in the existing equilibrium between the different As species. Thus, at very high $As^{(III)}$ concentrations, the band at 525 cm^{-1} ascribed to the As–O–As bonds, due to the formation of polymeric species, was absent under neutral and acidic conditions, although it appears strongly overlapped and blue-shifted at alkaline pHs (Fig. 3 A, B). Nonetheless, the Raman spectra of the saturated $As^{(III)}$ solutions (As_2O_3) show also a very broad band in the region 340-400 cm^{-1}, which also ascribes probably to As_4O_6 tetrameric species, particularly present in the cubic structure of solid arsenolite [56]. This assumption derived from the Raman spectra of the dry precipitate obtained from the As_2O_3 solutions at pH 11.2 and 8.9 (Fig. 4B), which show Raman shifts at 443 cm^{-1} and 412 cm^{-1} ascribed to the Raman modes of E_g and T_{2g}, respectively, and established for arsenolite [56]. In any case, the possible presence of small size

polymeric species, such as dimers or trimers in the saturated $As^{(III)}$ solutions, could exist but be unresolved due to the strong overlapping between the peaks. By dehydration and at high concentrations of $As^{(III)}$ solutions, alternative polymeric species, such as As oxohydroxy oligomers, $As_3O_6(OH)_3$, $As_6O_6(OH)_6$ and As_4O_6, are also possible, probably generated according to some of the following tentative reactions,

$$nAs(OH)_3 \leftrightarrow \begin{cases} As_nO_{(n-1)}(OH)_{(n+2)} + (n-1)H_2O & (n=2) \\ As_nO_{(2n)}(OH)_n + nH_2O & (n=3) \\ As_nO_{(n+2)} + (n+2)H_2O & (n=4) \\ As_nO_n(OH)_n + nH_2O & (n=6) \end{cases} \quad (7)$$

Nonetheless, $As_3O_3(OH)_3$ is the most probable oligomeric species in solution.

Contrarily to the solid $As^{(III)}$ species, the Raman spectra of the solid $As^{(V)}$ species fit well those obtained from the $As^{(V)}$ solutions. Furthermore, essential differences in the Raman spectra of the dry precipitates depends on the original $As^{(III)}$ solution pH. The dry residue As(III) species' Raman spectra show many thin Raman peaks, representing minor interactions with water (solvent). The Raman spectra of the precipitates with some moiety degree clarify this behaviour (Fig. 6 A, B and Fig. 7 A, B).

The availability of experimental $As^{(V)}/As^{(III)}$ Raman spectra in diluted solutions allows us to assess in detail the protocol's performance employed to include solvent effects into the Raman spectra calculations. We carried out DFT calculations on solute-water clusters built-in in the solvent continuum described by the well-known PCM method. We generated the clusters by classical molecular dynamics simulations assuming some conformational averaging. However, a trade-off between computational cost and accuracy is required, and, therefore, our approach considered only up to 100 clusters comprising ~6-8 water molecules each. Then we averaged first the spectra of all the clusters belonging to a given species followed by pH-

averaging, in which we weighed the various oxoacid spectra in terms of their calculated fractional concentrations. In general terms, the experimental and predicted spectra are in good agreement, validating thus the utility of the hybrid DFT approach. The statistical uncertainty and noise level also affect the theoretical Raman spectra due to limited sampling and truncation effects of cluster models. Other factors not considered in the calculations may relate to anharmonicity, differences in the spectral resolution and presence of other As species.

Clearly, the structures and Raman spectra of the oxoacid clusters emphasise the significant influence of the fluctuating solvent environment on the intensity, broadening, and displacement of maximum Raman activity (Figs. S2, S3 S4 and S5). As expected, the presence of the water molecules gives rise to a more significant number of theoretical Raman peaks in the 200-1000 cm^{-1} interval in the calculated spectra for the individual cluster models. Thus, the dispersion of the vibrational frequencies transforms the narrow Lorentzian peaks with a 4 cm^{-1} FWHM into broader bands with ~100 cm^{-1} and ~50 cm^{-1} width for As–OH and As–O stretching, respectively, the Raman activity of the bands being at least ~5-fold lower than those of the equivalent peaks in the absence of explicit water molecules. As noticed above, the As–OH vibrations are more prone to H-bond contacts, leading to a blue shifting between 5 and 20 cm^{-1} concerning the PCM spectra. The corresponding behaviour of the As–O peaks is particularly irregular: the most active As–O signals in $H_2AsO_4^-$ / $HAsO_4^{2-}$ show apparent red/blue shift by 10/20 cm^{-1}, the intense As–O peak/band in AsO_4^{3-} being blue shift by nearly 40 cm^{-1}.

For the averaged spectra of $As^{(V)}$, we checked the critical role of the protonation of the anionic species in the solution. Thus, the Raman activity significantly reduces by lowering the pH because the $As^{(V)}$ species become protonated (increasing the less active As-OH vibrations), shown in the calculated and experimental spectra. Ongoing to acidic solutions, it is noteworthy that activity of the As–OH band seems theoretically underestimated, as the intensity of the narrow experimental As–OH band in H_3AsO_4 is comparable to that of the As–O band in AsO_4^{3-}.

In the case of $As^{(III)}$ averaged spectra, it is also clear that the simulation overestimates the attenuation of the Raman scattering, especially for the As–OH bands, rendering pH-averaged spectra that have relatively low activity with a significant noise level. These effects might relate to an exaggerated solute-water/solvent coupling found in the frequency calculations on the cluster models. However, there is a good agreement with the experimental data concerning the positioning and relative activities of the bands.

Some of the Raman peaks of the As species, at each pH in solution and solid phase, show interesting potential analytical possibilities. Looking for any characteristic Raman peaks of the solid phases, we can derive a few of them from Table 2, where the peaks at 789 and 910 cm^{-1} directly associate with $As^{(V)}$ at pH 3.0. Other peaks at 1070 and 700 cm^{-1} (pH > 10), 472 (pH 9.0) and 186, 479 and 779 cm^{-1} (pH 6.0), might also be used for a qualitative identification of As_2O_3. Other characteristics peaks for other species are bolded in Tables 1 and 2.

Alternatively, the intensity of a few peaks grows linearly with the arsenic concentration in solution, showing some potential applicability for analytical purposes. The $As^{(III)}$ Raman peak at 700-721 cm^{-1}, assigned to the As–O stretch, offers an excellent linear relationship with the As_2O_3 concentration in the pH range of 0.0-9.0 and $NaAsO_2$ solutions at basic pH 6.0-9.0 (Fig. 4 A, B). The peak at 784 cm^{-1} (Fig. 2A) ascribes to the symmetric τ(As–O) mode for $As^{(V)}$ at pH 0.5, and it is also adequate at basic pH (12.0) but with minor sensitivity (Fig. 4 C). The following equation for As_2O_5 at pH 0.5 is helpful in the $[As_2O_5]$ concentration range between 0.1 M and 1.0 M,

$$I_{(764\ cm^{-1})} = (-1300.0 \pm 400.0) + (3300.0 \pm 700.0)\ [As_2O_5] \qquad (R^2 = 0.9990) \qquad (8)$$

Alternative equations were possible at other pHs and for other Raman peaks, although with smaller slopes (Table S8). Similarly, the following equation for $NaAsO_2$ at pH 9.0 can be used in the concentration range between 0.5 M and 3.0 M.

$$I_{(702\ cm^{-1})} = (1300.0\pm200.0) + (3000.0\pm100.0)\ [NaAsO_2] \qquad (R^2 = 0.99761) \qquad (9)$$

Nonetheless, a particular situation appears with NaH_2AsO_4 solutions because several peaks suffer strong shifts with pH.

4. Conclusions

Raman spectroscopy resulted very adequately to study the As oxoacids species in an aqueous solution and solid phase. The Raman spectra of the As aqueous solutions at different pHs show minor differences with the As concentration, whilst for increased As concentrations, especially in the solid phase, some polymeric species can form via hydrogen bridges.

Despite the presence of highly-charged species, conventional DFT calculations reasonably can reproduce the As oxoacid spectra in the aqueous solution provided that explicit solvent molecules are included in the models and some conformational averaging is performed. Some differences between theory and experiment arise in the positioning and relative intensity of the more critical peaks and the appearance of other low-intensity bands. Considering the significant coupling between the oxoacid and water molecules, more accurate predictions would require the inclusion of further explicit waters and incorporating anharmonicity effects.

On the other hand, helpful information is possible from the relationship between the Raman spectra of the As oxoacids in solution and solid phase. Raman spectra of the dry precipitates allow identifying indirectly molecular species in the corresponding aqueous

703 solutions. Further, some analytical applications were possible using the intensity and intensity
704 ratios of some Raman peaks.

705 **Author Contributions**

706 FJ Pereira: Methodology, Raman measurements, Reviewing, Supervision. R López:
707 Methodology, DFT Analysis, Reviewing, Supervision. D. Suárez: Methodology, DFT
708 Analysis, Reviewing. AJ Aller: Conceptualisation, Writing-Reviewing and Editing. FJ Pereira
709 and R López contributed equally and supervised all the tasks of the manuscript. All authors
710 reviewed this manuscript.

711 **Acknowledgements**

712 We produced molecular graphics images using the UCSF Chimera package from the
713 Resource for Biocomputing, Visualization, and Informatics at the University of California, San
714 Francisco (supported by NIH P41 RR-01081). We acknowledge support by the PGC2018-
715 095953-B grant (MICINN, Spain), but this research did not receive any specific grant from
716 funding agencies in the commercial or not-for-profit sectors.

717 **Conflict of Interest**

718 The authors declare that they have no conflict of interest.

719 **References**

720 [1] H.A. Szymanski, L. Marabella, J. Hoke, J. Harter, Infrared and Raman studies of
721 arsenic compounds, Appl. Spectrosc. 22 (1968) 297–304.

722 [2] M. Rojas-López, J.M. Gracia-Jiménez, M.A. Vidal, H. Navarro-Contreras, R. Silva-
723 González, E. Gómez, Raman study of luminescent spark processed porous GaAs, J.
724 Vac. Sci. Technol. B Microelectron. Nanom. Struct. 19 (2001) 622.
725 doi:10.1116/1.1366709.

[3] S.L. Soignet, S.R. Frankel, D. Douer, M.S. Tallman, H. Kantarjian, E. Calleja, et al., United States multicenter study of arsenic trioxide in relapsed acute promyelocytic leukemia, J. Clin. Oncol. 19 (2001) 3852–3860. doi:10.1200/JCO.2001.19.18.3852.

[4] J.O. Jensen, S.J. Gilliam, A. Banerjee, D. Zeroka, S.J. Kirkby, C.N. Merrow, A theoretical study of As4O6: Vibrational analysis, infrared and Raman spectra, J. Mol. Struct. THEOCHEM. 664–665 (2003) 145–156. doi:10.1016/j.theochem.2003.08.109.

[5] G. Cassone, D. Chillé, C. Foti, O. Giuffré, R.C. Ponterio, J. Sponer, et al., stability of hydrolytic arsenic species in aqueous solutions: As3+ vs. As5+, Phys. Chem. Chem. Phys. 20 (2018) 23272–23280. doi:10.1039/c8cp04320e.

[6] K. Müller, V.S.T. Ciminelli, M.S.S. Dantas, S. Willscher, A comparative study of As(III) and As(V) in aqueous solutions and adsorbed on iron oxy-hydroxides by Raman spectroscopy, Water Res. 44 (2010) 5660–5672. doi:10.1016/j.watres.2010.05.053.

[7] J.A. Tossell, M.D. Zimmermann, calculation of the structures, stabilities, and vibrational spectra of arsenites, thioarsenites and thioarsenates in aqueous solution, Geochim. Cosmochim. Acta. 72 (2008) 5232–5242. doi:10.1016/J.GCA.2008.08.013.

[8] E.E. Zvereva, A.R. Shagidullin, S.A. Katsyuba, Ab initio and DFT predictions of infrared intensities and raman activities, J. Phys. Chem. A. 115 (2011) 63–69. doi:10.1021/JP108057P.

[9] I. Dhouib, P. Guionneau, Z. Elaoud, Vibrational spectroscopy, electrical characterisation, nonlinear optical properties and DFT calculation of (NEt4)(H2AsO4)(H3AsO4)2, J. Coord. Chem. 70 (2017) 3585–3597. doi:10.1080/00958972.2017.1406082.

[10] M. Yang, Y. Sun, X. Zhang, B. McCord, A.J. McGoron, A. Mebel, et al., Raman spectra of thiolated arsenicals with biological importance, Talanta. 179 (2018) 520–530. doi:10.1016/j.talanta.2017.11.022.

[11] S.T. Mutter, F. Zielinski, P.L.A. Popelier, E.W. Blanch, Calculation of Raman optical activity spectra for vibrational analysis, Analyst. 140 (2015) 2944–2956. doi:10.1039/C4AN02357A.

[12] M. Thomas, M. Brehm, R. Fligg, P. Vöhringer, B. Kirchner, Computing vibrational

spectra from ab initio molecular dynamics, Phys. Chem. Chem. Phys. 15 (2013) 6608–6622. doi:10.1039/C3CP44302G.

[13] R.D. Johnson III, NIST Computational Chemistry Comparison and Benchmark Database, NIST Stand. Ref. Database Number 101. (n.d.). doi:10.18434/T47C7Z.

[14] M.J. Frisch, G.W. Trucks, H.B. Schlegel, G.E. Scuseria, M.A. Robb, J.R. Cheeseman, et al., Gaussian 16, Revision C.01, Gaussian, Inc. (2016).

[15] A.D. Becke, Density-functional thermochemistry. III. The role of exact exchange, J. Chem. Phys. 98 (1993) 5648–5652. doi:10.1063/1.464913.

[16] C. Lee, W. Yang, R.G. Parr, Development of the Colle-Salvetti correlation-energy formula into a functional of the electron density, Phys. Rev. B. 37 (1988) 785–789. doi:10.1103/PhysRevB.37.785.

[17] J.P. Perdew, K. Burke, Generalised gradient approximation for the exchange-correlation hole of a many-electron system, Phys. Rev. B - Condens. Matter Mater. Phys. 54 (1996) 16533–16539. doi:10.1103/PhysRevB.54.16533.

[18] J. Da Chai, M. Head-Gordon, Long-range corrected hybrid density functionals with damped atom-atom dispersion corrections, Phys. Chem. Chem. Phys. 10 (2008) 6615–6620. doi:10.1039/b810189b.

[19] J. Da Chai, M. Head-Gordon, Systematic optimisation of long-range corrected hybrid density functionals, J. Chem. Phys. 128 (2008) 84106. doi:10.1063/1.2834918.

[20] T.H. Dunning, Gaussian basis sets for use in correlated molecular calculations. I. The atoms boron through neon and hydrogen, J. Chem. Phys. 90 (1989) 1007–1023. doi:10.1063/1.456153.

[21] K.A. Peterson, T.H. Dunning, Accurate correlation consistent basis sets for molecular core-valence correlation effects: The second row atoms Al-Ar, and the first row atoms B-Ne revisited, J. Chem. Phys. 117 (2002) 10548–10560. doi:10.1063/1.1520138.

[22] D.E. Woon, T.H. Dunning, Gaussian basis sets for use in correlated molecular calculations. V. Core-valence basis sets for boron through neon, J. Chem. Phys. 103 (1995) 4572–4585. doi:10.1063/1.470645.

[23] A. Bauzá, I. Alkorta, A. Frontera, J. Elguero, On the reliability of pure and hybrid DFT

methods for the evaluation of halogen, chalcogen, and pnicogen bonds involving anionic and neutral electron donors, J. Chem. Theory Comput. 9 (2013) 5201–5210. doi:10.1021/ct400818v.

[24] A.D. Becke, Density-functional exchange-energy approximation with correct asymptotic behavior, Phys. Rev. A. 38 (1988) 3098–3100. doi:10.1103/PhysRevA.38.3098.

[25] J. Tomasi, B. Mennucci, E. Cance?s, The IEF version of the PCM solvation method: An overview of a new method addressed to study molecular solutes at the QM ab initio level, J. Mol. Struct. THEOCHEM. 464 (1999) 211–226.

[26] C.S. Pomelli, J. Tomasi, V. Barone, An improved iterative solution to solve the electrostatic problem in the polarisable continuum model, Theor. Chem. Acc. 105 (2001) 446–451.

[27] G. Scalmani, M.J. Frisch, Continuous surface charge polarisable continuum models of solvation. I. General formalism, J. Chem. Phys. 132 (2010) 114110. doi:10.1063/1.3359469.

[28] S. Corni, C. Cappelli, R. Cammi, J. Tomasi, Theoretical Approach to the Calculation of Vibrational Raman Spectra in Solution within the Polarisable Continuum Model, J. Phys. Chem. A. 105 (2001) 8310–8316. doi:10.1021/jp011079c.

[29] W.L. Jorgensen, J. Chandrasekhar, J.D. Madura, R.W. Impey, M.L. Klein, Comparison of simple potential functions for simulating liquid water, J. Chem. Phys. 79 (1983) 926–935. doi:doi:http://dx.doi.org/10.1063/1.445869.

[30] J. Wang, R.M. Wolf, J.W. Caldwell, P.A. Kollman, D.A. Case, Development and testing of a general amber force field, J Comput Chem. 25 (2004) 1157–1174. doi:10.1002/jcc.20035.

[31] J. Wang, W. Wang, P.A. Kollman, D.A. Case, Automatic atom type and bond type perception in molecular mechanical calculations, J Mol Graph Model. 25 (2006) 247–260. doi:10.1016/j.jmgm.2005.12.005.

[32] R. Salomon-Ferrer, D.A. Case, R.C. Walker, An overview of the Amber biomolecular simulation package, Wiley Interdiscip. Rev. Comput. Mol. Sci. 3 (2013) 198–210. doi:10.1002/wcms.1121.

[33] I.Y.B.-S. D.A. Case S.R. Brozell, D.S. Cerutti, T.E. Cheatham, III, V.W.D. Cruzeiro, T.A. Darden, R.E. Duke, D. Ghoreishi, M.K. Gilson, H. Gohlke, A.W. Goetz, D. Greene, R Harris, N. Homeyer, S. Izadi, A. Kovalenko, T. Kurtzman, T.S. Lee, S. LeGrand, P. Li, C. Lin, AMBER 2018, (2018).

[34] T. Lu, F. Chen, Multiwfn: A multifunctional wavefunction analyser, J. Comput. Chem. 33 (2012) 580–592. doi:10.1002/jcc.22885.

[35] P.G. Seybold, Quantum chemical estimation of the acidities of some inorganic oxoacids, Mol. Phys. 113 (2015) 232–236. doi:10.1080/00268976.2014.927080.

[36] A. Guesmi, M. Nespolo, A. Driss, Synthesis, crystal structure and charge distribution of Na7As11O31: An oxygen-deficient layered sodium arsenate, J. Solid State Chem. 179 (2006) 2466–2471. doi:10.1016/j.jssc.2006.04.010.

[37] S.C.B. Myneni, S.J. Traina, G.A. Waychunas, T.J. Logan, Experimental and theoretical vibrational spectroscopic evaluation of arsenate coordination in aqueous solutions, solids, and at mineral-water interfaces, Geochim. Cosmochim. Acta. 62 (1998) 3285–3300. doi:10.1016/S0016-7037(98)00222-1.

[38] K.D. zur Loye, A.M. Latshaw, M.D. Smith, W.M. Chance, H.-C. zur Loye, Synthesis and Crystal Structure of Sodium Arsenate Oxyhydroxide: Na4(AsO4)OH, J. Chem. Crystallogr. 45 (2015) 20–25. doi:10.1007/s10870-014-0558-7.

[39] J. Ring, L. Lindenthal, M. Weil, B. Stöger, Crystal structure of sodium dihydrogen arsenate, Acta Crystallogr. Sect. E Crystallogr. Commun. 73 (2017) 1520–1522. doi:10.1107/S2056989017013470.

[40] J. Mähler, I. Persson, R.B. Herbert, Hydration of arsenic oxyacid species, Dalt. Trans. 42 (2013) 1364–1377. doi:10.1039/c2dt31906c.

[41] N.R. Council, Arsenic, in: N.R. Council (Ed.), Med. Biol. Eff. Environ. Pollut., The National Academic Press, Washington, D.C., 1977. doi:https://doi.org/10.17226/9003.

[42] F.J. Pereira, M.D. Vázquez, L. Debán, A.J. Aller, Inorganic arsenic speciation by differential pulse anodic stripping voltammetry using thoria nanoparticles-carbon paste electrodes, Talanta. 152 (2016) 211–218. doi:10.1016/j.talanta.2016.02.011.

[43] F.J. Pereira, M.D. Vázquez, L. Debán, A.J. Aller, Cyclic voltammetry of arsenic-doped cysteine-capped ceramic nanoparticles, Electrochim. Acta. 109 (2013) 125–135.

doi:10.1016/j.electacta.2013.07.087.

[44] M.A. Hasnat, M.M. Hasan, N. Tanjila, M.M. Alam, M.M. Rahman, pH dependent kinetic insights of electrocatalytic arsenite oxidation reactions at Pt surface, Electrochim. Acta. 225 (2017) 105–113. doi:10.1016/j.electacta.2016.12.055.

[45] P.A. Guńka, K. Kraszewski, Y.S. Chen, J. Zachara, The structure and energetics of arsenic(iii) oxide intercalated by ionic azides, Dalt. Trans. 43 (2014) 12776–12783. doi:10.1039/c4dt01569j.

[46] M. Yang, V. Liamtsau, C. Fan, K.L. Sylvers, A.J. McGoron, G. Liu, et al., Arsenic Speciation on Silver Nanofilms by Surface-Enhanced Raman Spectroscopy, Anal. Chem. 91 (2019) 8280–8288. doi:10.1021/acs.analchem.9b00999.

[47] S. Xu, F.P. Sabino, A. Janotti, D.B. Chase, D.L. Sparks, J.F. Rabolt, Unique Surface Enhanced Raman Scattering Substrate for the Study of Arsenic Speciation and Detection, J. Phys. Chem. A. 122 (2018) 9474–9482. doi:10.1021/acs.jpca.8b09104.

[48] A. Ramírez-Solís, J.I. Amaro-Estrada, C.I. León-Pimentel, J. Hernández-Cobos, S.E. Garrido-Hoyos, H. Saint-Martin, On the aqueous solvation of AsO(OH)3: Vs. As(OH)3. Born-Oppenheimer molecular dynamics density functional theory cluster studies, Phys. Chem. Chem. Phys. 20 (2018) 16568–16578. doi:10.1039/c8cp01673a.

[49] F.K. Vansant, B.J. Van Der Veken, H.O. Desseyn, Vibrational analysis of arsenic acid and its anions, J. Mol. Struct. 15 (1973) 425–437. doi:10.1016/0022-2860(73)80012-2.

[50] S. Goldberg, C.T. Johnston, Mechanisms of arsenic adsorption on amorphous oxides evaluated using macroscopic measurements, vibrational spectroscopy, and surface complexation modeling, J. Colloid Interface Sci. 234 (2001) 204–216. doi:10.1006/jcis.2000.7295.

[51] C. Outeiral, M.A. Vincent, Á. Martín Pendás, P.L.A. Popelier, Revitalising the concept of bond order through delocalisation measures in real space, Chem. Sci. 9 (2018) 5517–5529. doi:10.1039/c8sc01338a.

[52] G. Lendvay, On the correlation of bond order and bond length, J. Mol. Struct. THEOCHEM. 501–502 (2000) 389–393. doi:10.1016/S0166-1280(99)00449-2.

[53] R. Gout, G. Pokrovski, J. Schott, A. Zwick, Raman spectroscopic study of arsenic speciation in aqueous solutions up to 275°C, J. Raman Spectrosc. 28 (1997) 725–730.

doi:10.1002/(SICI)1097-4555(199709)28:9<725::AID-JRS169>3.0.CO;2-9.

[54] G.S. Pokrovski, J.M. Bény, A. V. Zotov, Solubility and Raman spectroscopic study of as(III) speciation in organic compound-water solutions. A hydration approach for aqueous arsenic in complex solutions, J. Solution Chem. 28 (1999) 1307–1327. doi:10.1023/A:1021795924067.

[55] T.M. Loehr, R.A. Plane, Raman spectra and structures of arsenious acid and arsenites in aqueous solution, Inorg. Chem. 7 (1968) 1708–1714. doi:10.1021/ic50067a004.

[56] S.J. Gilliam, C.N. Merrow, S.J. Kirkby, J.O. Jensen, D. Zeroka, A. Banerjee, Raman spectroscopy of arsenolite: Crystalline cubic As4O6, J. Solid State Chem. 173 (2003) 54–58. doi:10.1016/S0022-4596(03)00082-3.

886 **Table 1.** The primary Raman shifts from aqueous solutions.

pH	As_2O_3	$NaAsO_2$	As_2O_5	Na_2HAsO_4
0.3	**700**, 650sh	**701**, 651, 408	**932**, ***764, 345***	**932**, ***764, 340***
3.0	**700**, 650sh	**701**, 651, 408	**877**, **745**, 367	**878**, **746**, 368
7.0	**700**, 650sh	**701**, 651, 408	**838**, 745, 700, 380, 345, 325	870sh, **842**, 745↓, 700, 382, 345
9.5	793, **700**, 586, 340	**784**, **712**, 651, 535, 317	**838**, 700, 393, 334	**840**, 700, 386, 326
10.5		1065, 784, **712**, 575, 317		
12.0	**793**, **586**, 340	1065↓, **784**, **575**, 317	**815**, 408, 350	**815**, 410, 349

887

888 **Table 2.** Main Raman shifts of the dry precipitates.

pH	As_2O_3	$NaAsO_2$	As_2O_5	Na_2HAsO_4
0.3	779, 555, 479, 378, 269, 186	Fluorescence	**930sh**, 860, ***774***, 400, ***343***, 270	**930sh**, 870, ***773***, 380, ***344***, 270
3.0	779↓, 555, 479, 378, 269, 186	Fluorescence	**904**, 850sh, 833, 809, **740**, 420sh, 382, 343, 320, 150	**910**, **789**, 770, 433, 380, 340, 302, 180, 140
5.0-7.0	**779**, 555, 525, **479**, 415, 378, 360, 269, **186**, 108	**785**, 561, **472**, 370, **269**, 183	**911**, **789**, 774, 432, 385, 343, **303**, 180, 140	905, **870**, 840, 808, 721, 433sh, 402sh, 380, 340
9.5	**828**, **750**, 643, 560, 503, **472**, 412, 360, 336, 280, 253, 216, 171sh, 143, 125↓, 108	**785**, 566, **472**, 370, **269**, **183**	**840sh**, **809**, 740, 400, 382, 343, 320, 180, 140	**841**, **808**, 740, 420sh, 402, 378, 344, 318, 180, 140
12.0	**1072**, **843**, **700**, 560, 519, 445, 380↓, 336, 270, 242, 216, 171, 143, 125sh, 108	**1070**, **843**, **785↓**, **700**, 566, 518, 428, 370↓, 355, 270, 243, 220↓, 167, 142, 108	**821**, 790sh, 400, 343, 180	**1065↓**, **822**, 789sh, 770sh, 402, 344, 230, 180, 150

889

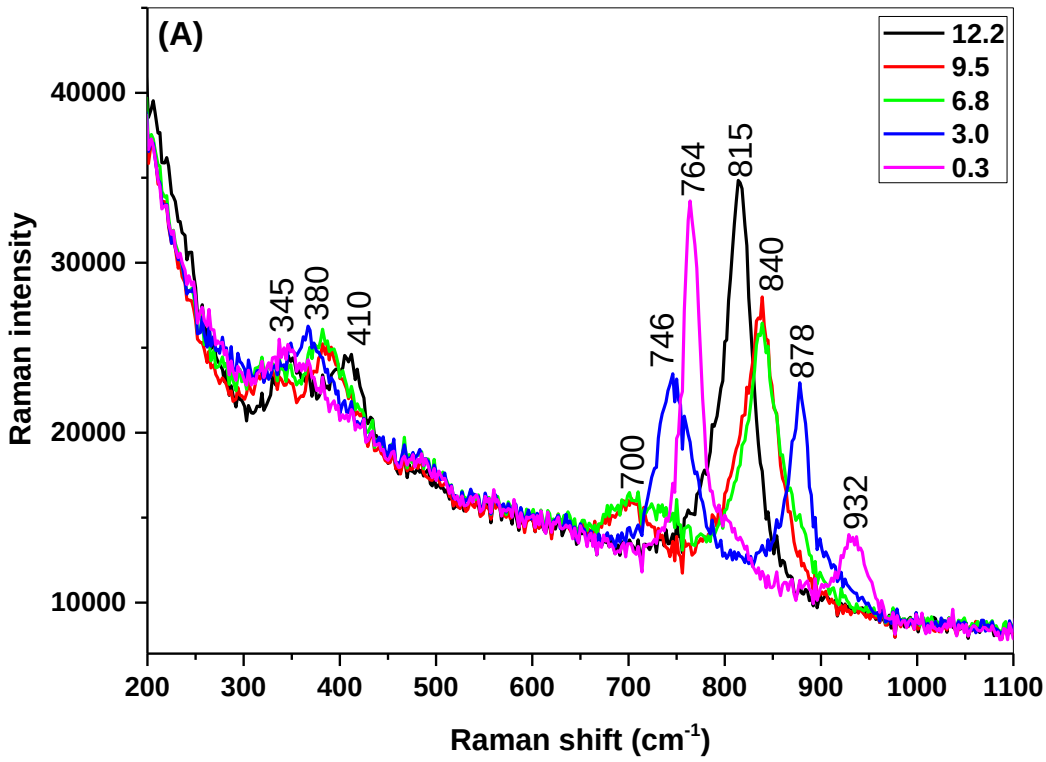

890

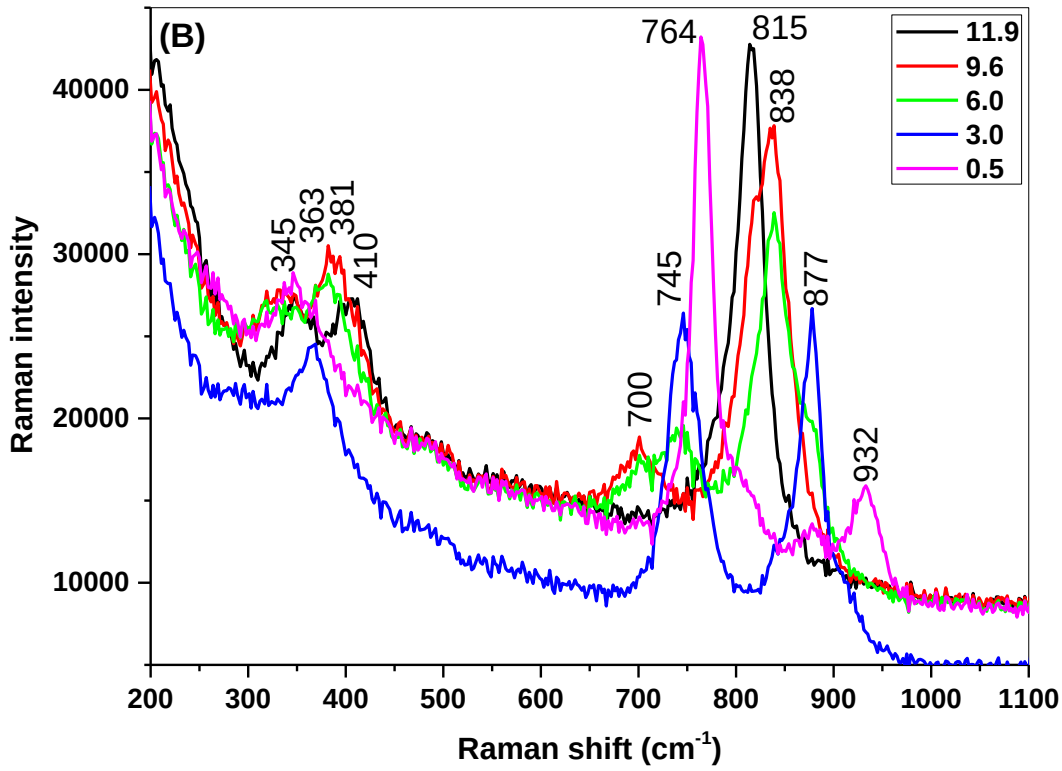

891

892 **Fig. 1.** Raman spectra of the Na_2HAsO_4 (A) and As_2O_5 (B) solutions at different pHs.

893

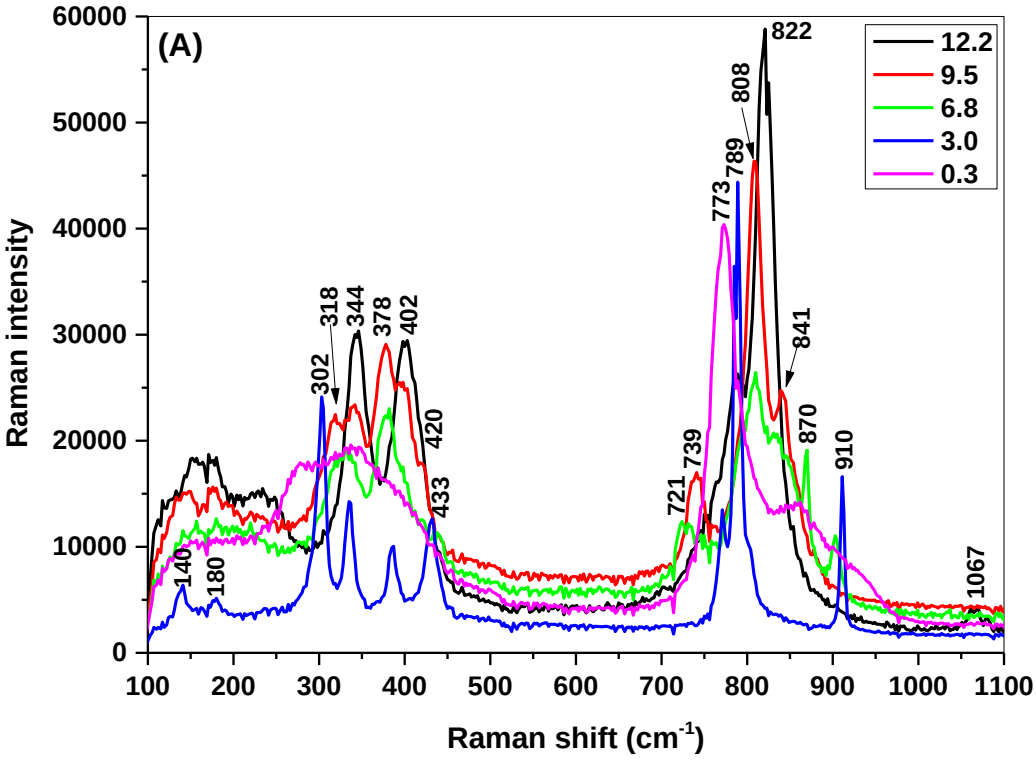

894

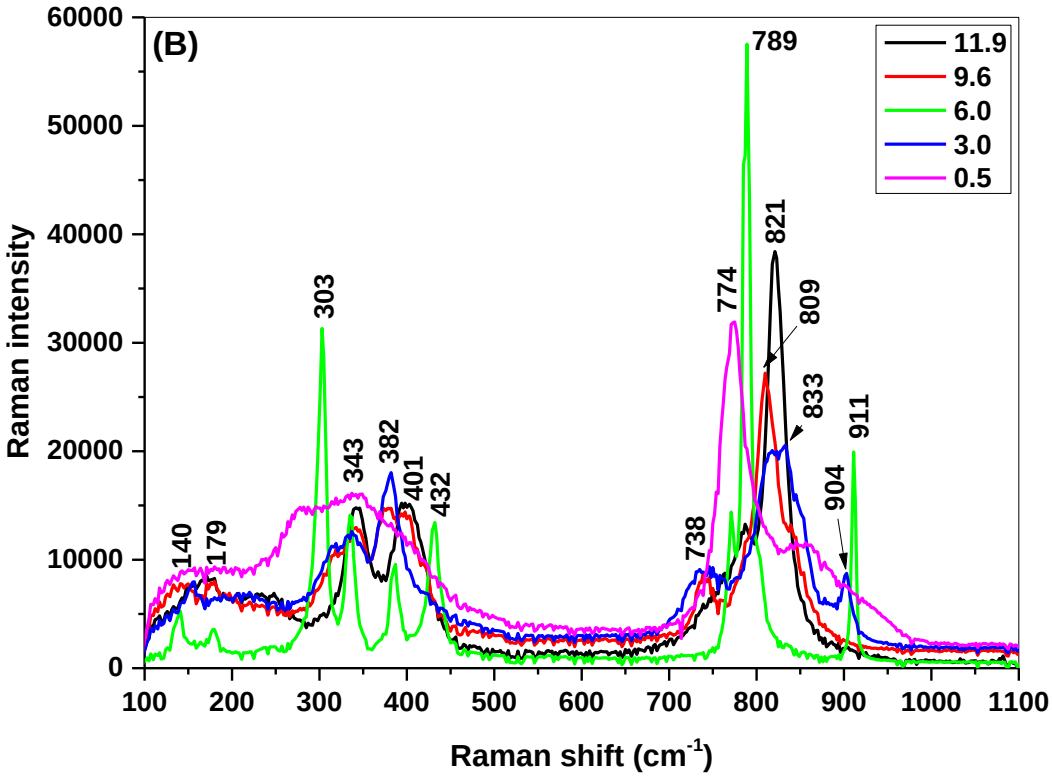

895

896 **Fig. 2.** Raman spectra of the dry Na_2HAsO_4 (A) and As_2O_5 (B) precipitates at different pHs.

897

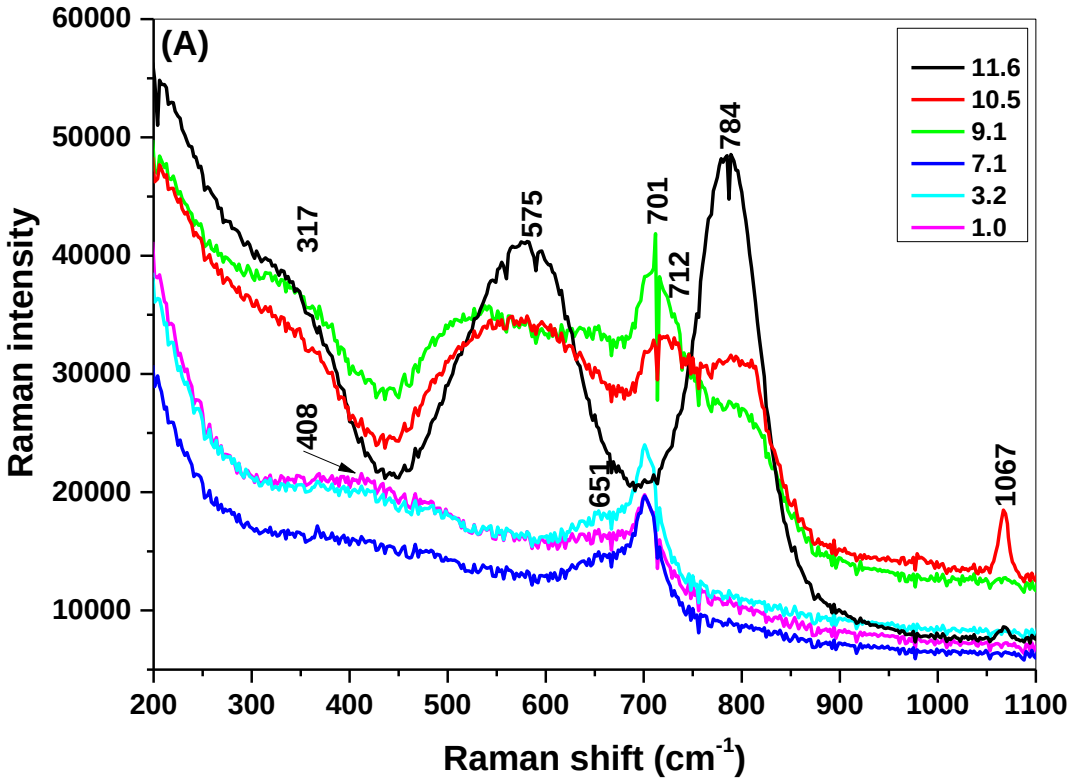

898

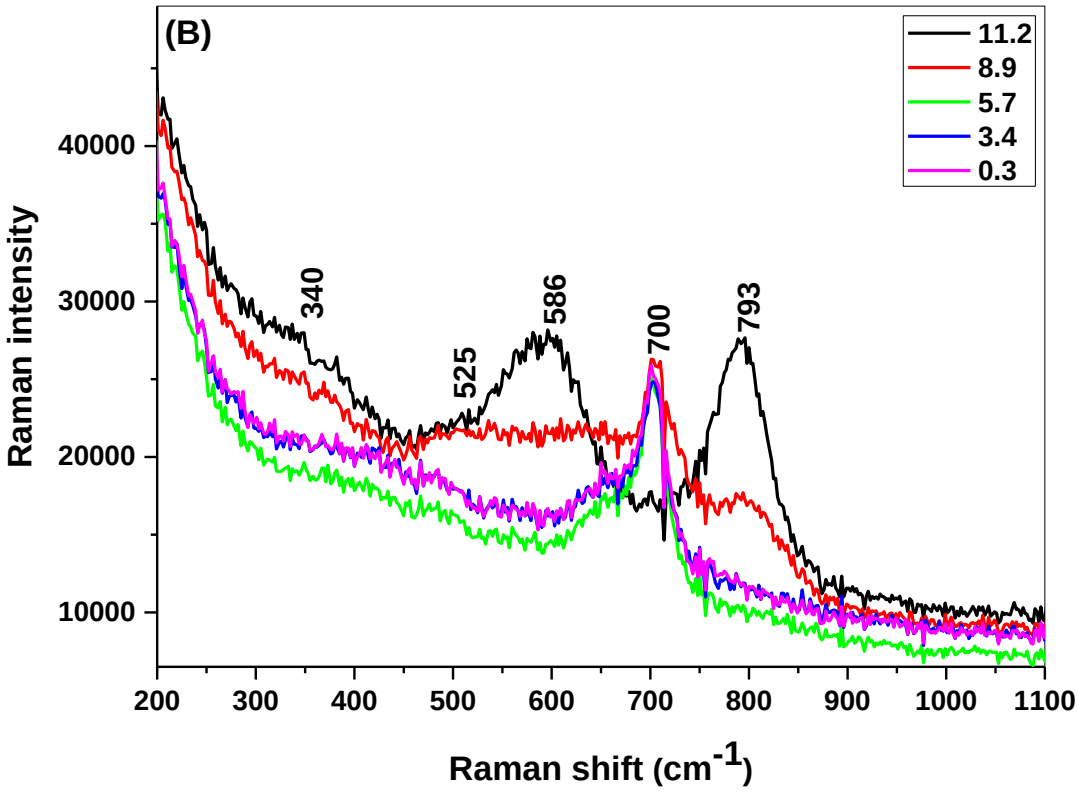

899

900 **Fig. 3.** Raman spectra of the $NaAsO_2$ (A) and As_2O_3 (B) solutions at different pHs.

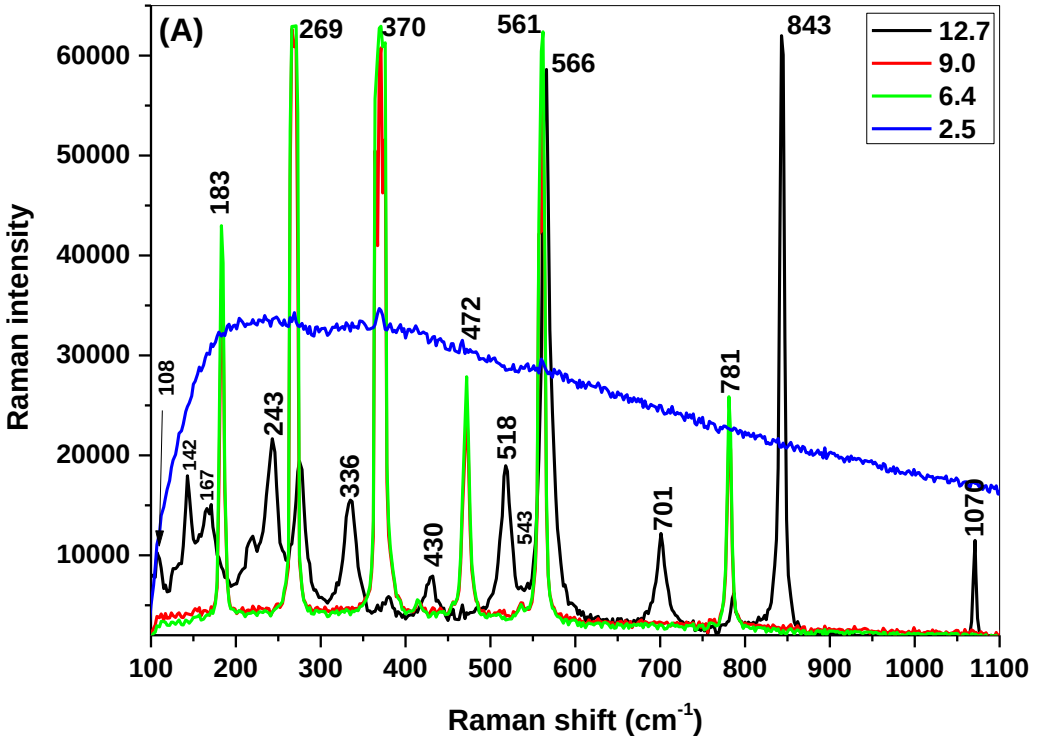

901

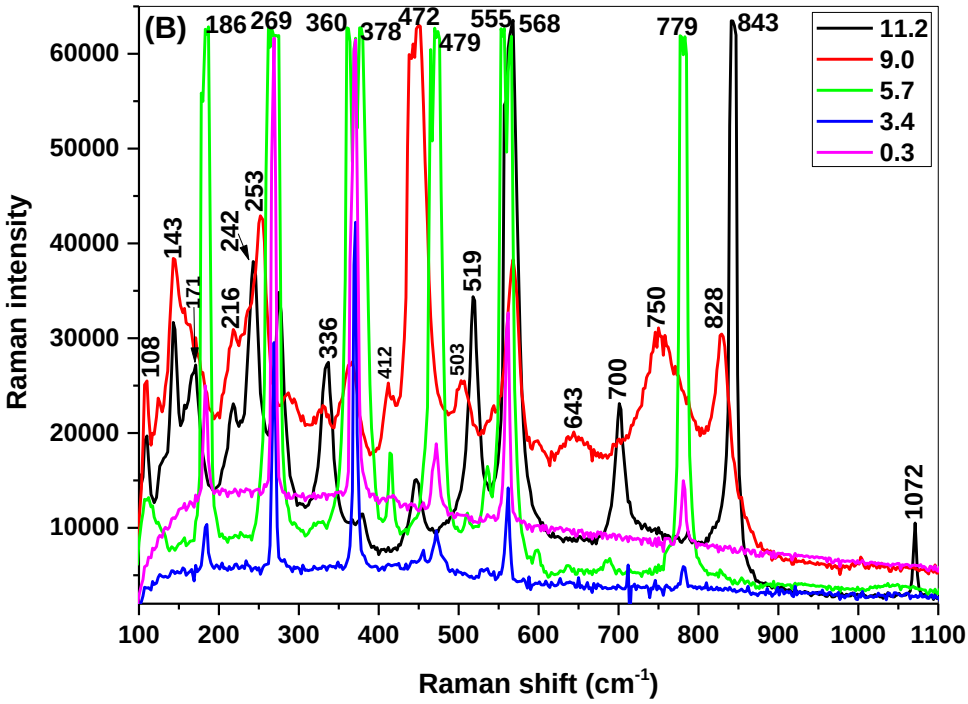

902

903 **Fig. 4.** Raman spectra of the dry $NaAsO_2$ (A) and As_2O_3 (B) precipitates at different pHs.

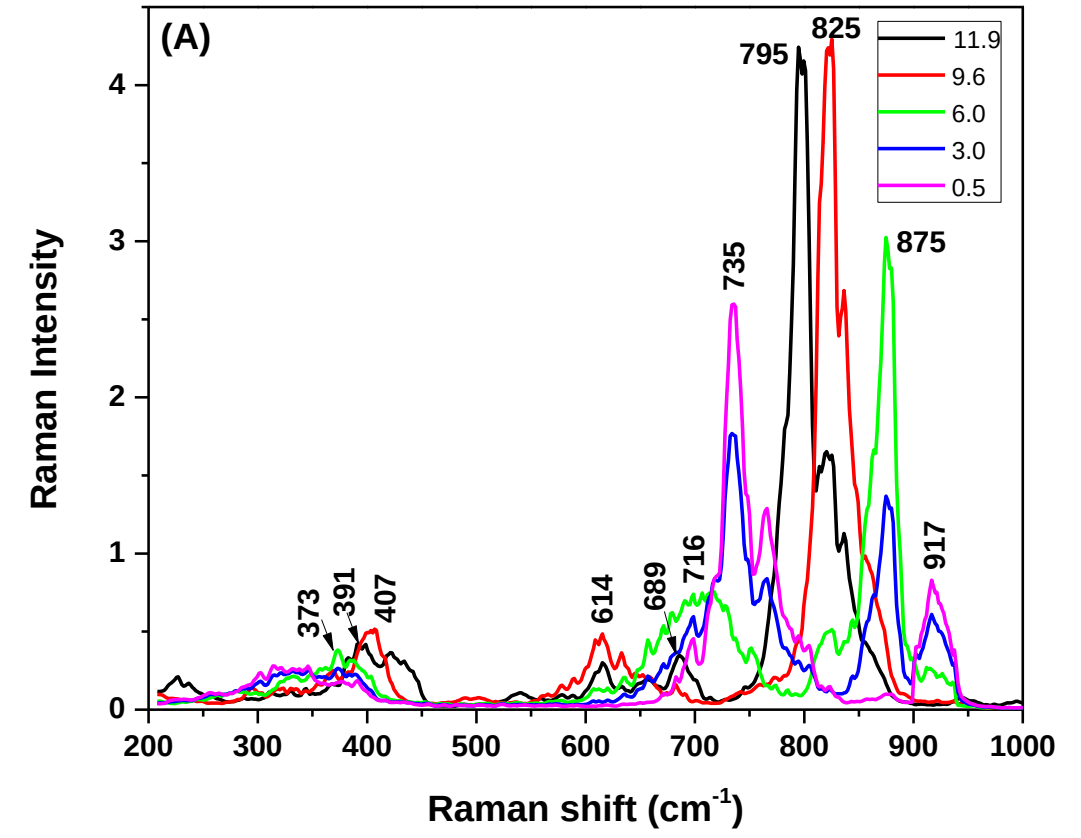

904

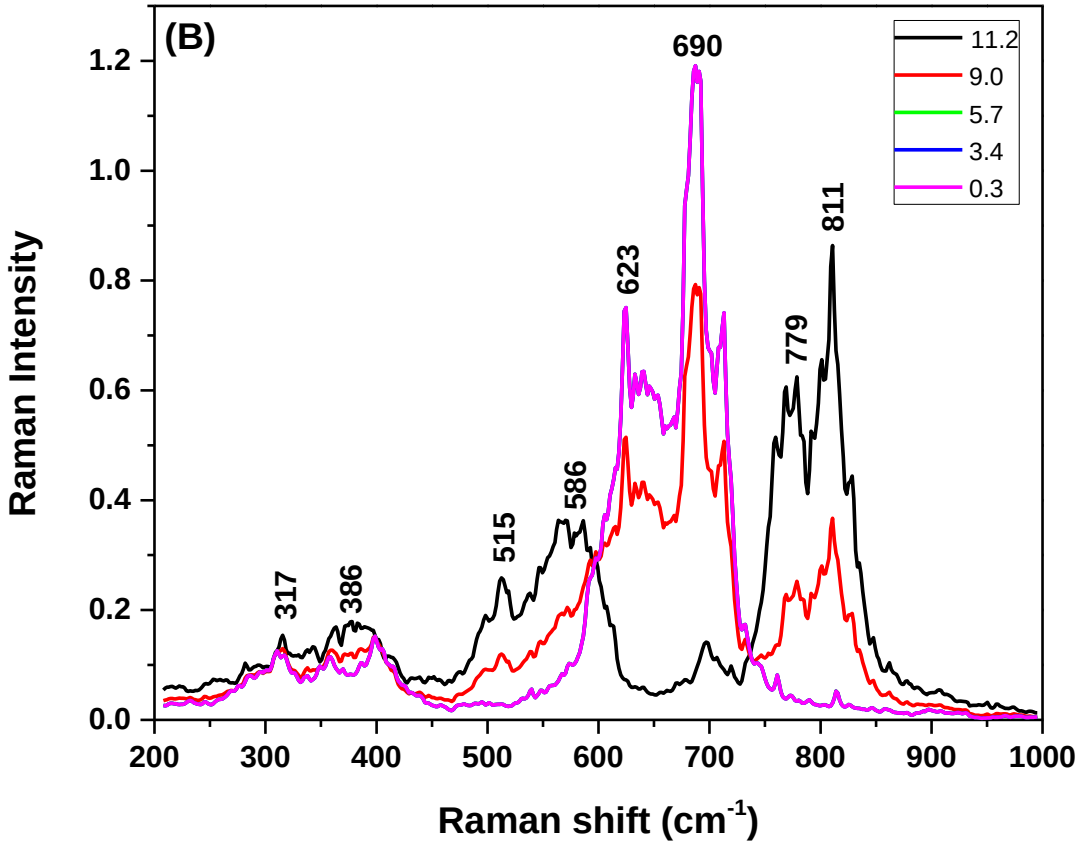

905

906 **Fig. 5.** Theoretical Raman spectra of the $As^{(V)}$ (A) and $As^{(III)}$ (B) oxoacids at different pHs
907 obtained via computational simulation.

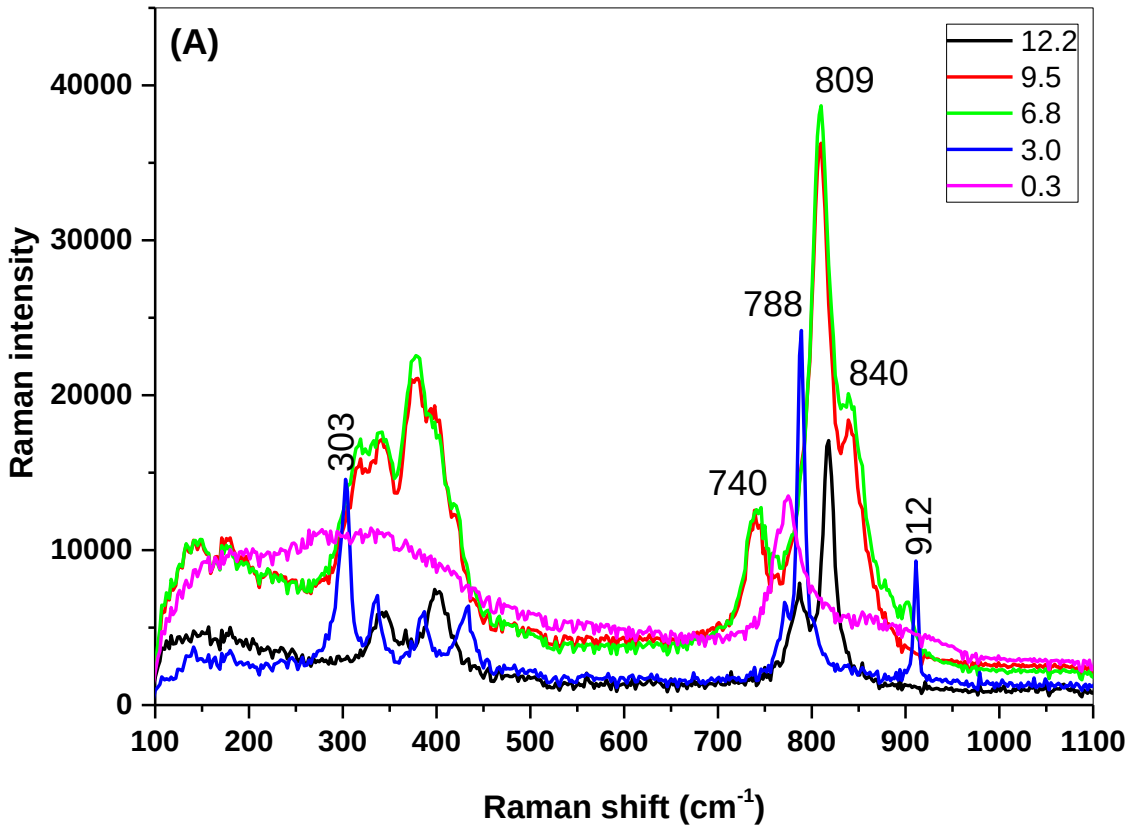

908

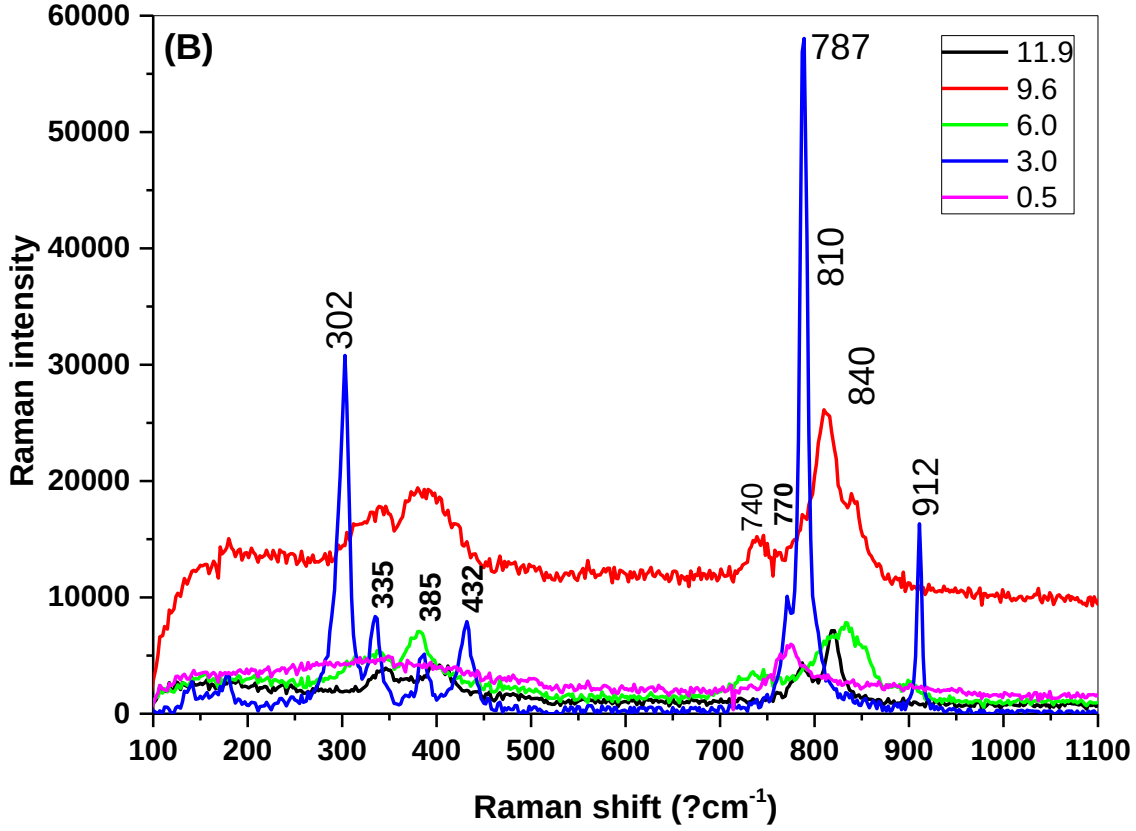

909

910 **Fig. 6.** Raman spectra of the wet Na_2HAsO_4 (A) and As_2O_5 (B) precipitates at different pHs.

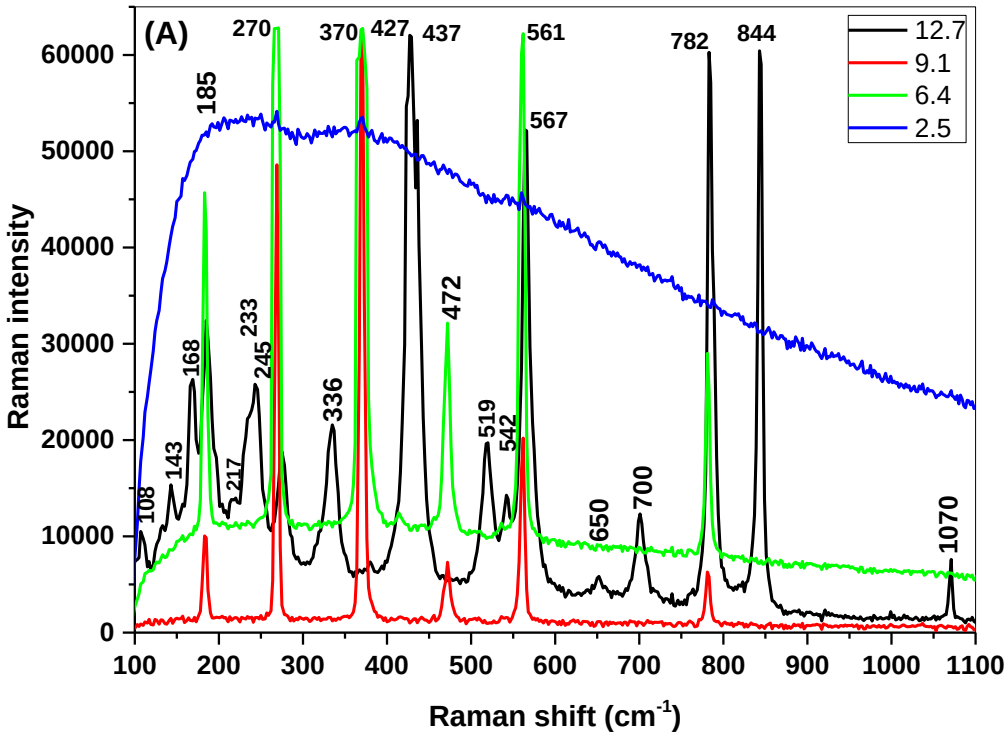

911

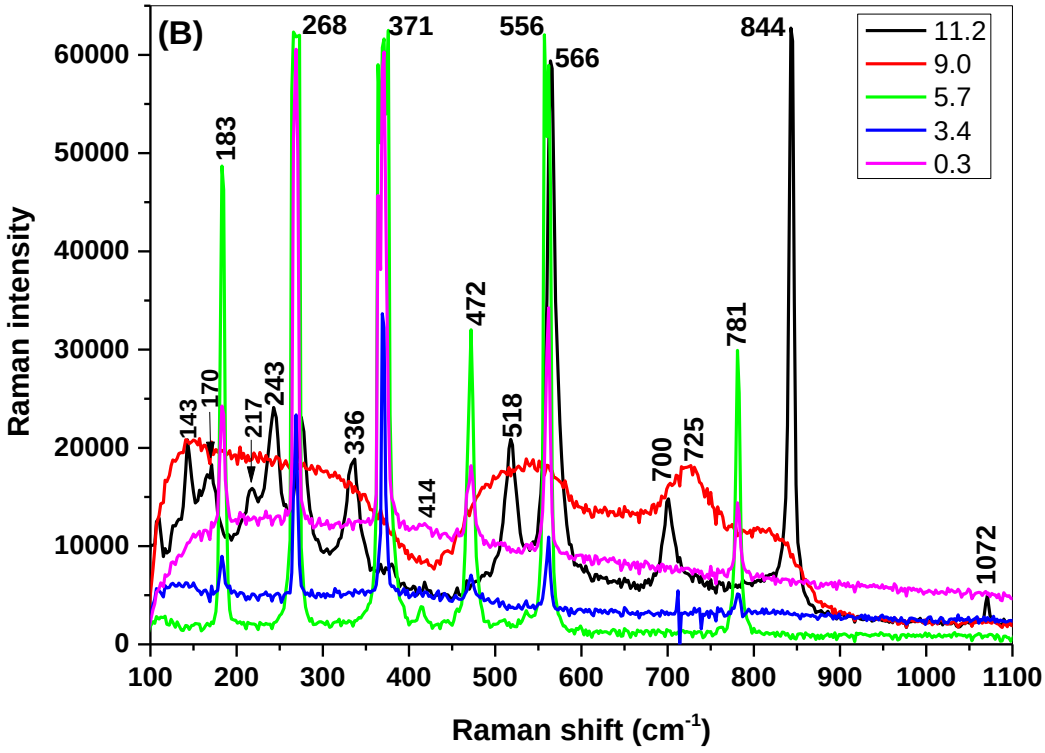

912

913 **Fig. 7.** Raman spectra of the wet $NaAsO_2$ (A) and As_2O_3 (B) precipitates at different pHs.